# Interannual to decadal variability of phosphate in the Oyashio region: Roles of wind-driven ocean current and tidally induced vertical mixing in the Sea of Okhotsk

Progress in Oceanography 197 (2021) 102615

Contents lists available at ScienceDirect

Progress in Oceanography

journal homepage: www.elsevier.com/locate/pocean

# Interannual to decadal variability of phosphate in the Oyashio region: Roles of wind-driven ocean current and tidally induced vertical mixing in the Sea of Okhotsk

Takuya Nakanowatari[a,*], Tomohiro Nakamura[b], Humio Mitsudera[b], Jun Nishioka[b], Hiroshi Kuroda[a], Keisuke Uchimoto[c]

[a] Fisheries Resources Institute, Japan Fisheries Research and Education Agency, Kushiro, Hokkaido 085-0802, Japan
[b] Pan-Okhotsk Research Center, Institute of Low Temperature Science, Hokkaido University, Sapporo 060-0819, Japan
[c] Research Institute of Innovative Technology for the Earth, Kizugawa 619-0292, Japan

ARTICLE INFO

*Keywords:*
Biogeochemical model
Phosphate
HNLC region
Arrested topographic wave
West Pacific pattern
18.6-year cycle

ABSTRACT

In the Oyashio region, remarkable climatic signals are observed in biogeochemical parameters such as phosphate ($PO_4$) concentration and debate continues regarding possible causes. Using a regional ice–ocean coupled model with a simple biogeochemical cycle, this study investigated the mechanisms controlling interannual–decadal variations in surface $PO_4$ in the Oyashio region and their relationships to climate change. Hindcast experiments forced with atmospheric reanalysis data for 1980–2010 and 18.6-year tidal mixing strength in the Kuril Straits qualitatively simulated interannual–decadal variations of surface $PO_4$, including a realistic seasonal cycle. Interannual fluctuations of simulated $PO_4$ in the Oyashio region are prominent in winter and characterized by year-to-year variability. Budget analysis of $PO_4$ in the mixed layer showed that the wintertime increase in $PO_4$ is caused by lateral advection as well as by local vertical convection. The geostrophic current variability responsible for lateral advection of $PO_4$ is related primarily to the barotropic response of arrested topographic waves in the Sea of Okhotsk as well as the wind-driven gyre in the North Pacific, both of which are regulated by the strength of the wintertime monsoon atmospheric pattern. On a decadal timescale (>7 years), temporal variations of surface $PO_4$ in the Oyashio region are characterized by decadal-scale fluctuation with positive (negative) peaks around 1985, 1995, and 2005 (1990 and 2000). A series of sensitivity experiments demonstrated that the decadal variability of $PO_4$ is largely explained by atmospheric wind conditions; however, modulation by 18.6-year tidal mixing is not negligible. Diagnostic analysis of wind-forced-experiment data revealed that the decadal $PO_4$ signal is advected from the Sea of Okhotsk, where 8-year leading wintertime Ekman upwelling supplies $PO_4$-rich water in the northern shelf region, and that the responsible atmospheric circulation is related to the West Pacific pattern. Our model simulation suggests that the wintertime wind-driven current system in the Sea of Okhotsk is important to the system feeding surface nutrients into the Oyashio region on an interannual–decadal timescale.

## 1. Introduction

The Oyashio is the western boundary current of the subarctic gyre in the North Pacific extending from the Kuril Straits to the east coast of the island of Hokkaido, Japan. Oyashio water is characterized as cold, low-salinity, and nutrient-rich water that is distinguishable from the relatively warm and more saline water of the East Kamchatka Current upstream. The Oyashio current intrudes southward along the offshore region of Hokkaido (hereafter, called the Oyashio region), where massive diatom blooms occur every spring (Kasai et al., 1997; Chiba et al., 2004; Tadokoro et al., 2005; Tsuda et al., 2005; Okamoto et al., 2010; Suzuki et al., 2011). Considerable primary production in the Oyashio region leads to substantial biological drawdown of $pCO_2$ (Takahashi et al., 2002; Nosaka et al., 2017) and supports the abundant fishery resources (Taniguchi, 1999; Sakurai, 2007). Therefore, comprehension of the mechanism of nutrient fluctuation in the Oyashio region is important for future projections of the climate and marine ecosystems.

* Corresponding author.
*E-mail address:* nakanowataritakuya@affrc.go.jp (T. Nakanowatari).

https://doi.org/10.1016/j.pocean.2021.102615
Received 16 July 2020; Received in revised form 17 March 2021; Accepted 28 May 2021
Available online 5 June 2021

The Oyashio region is also characterized by high-nutrient low-chlorophyll (HNLC) regions where dissolved Fe (dFe) limits phytoplankton growth (Tsuda et al., 2003; Harrison et al., 2004). The main sources of dFe in the Oyashio region are considered to be atmospheric dust derived from the Eurasian continent (Duce and Tindale, 1991; Mahowald et al., 2005; Measures et al., 2005) and oceanic flux from the continental shelf of the Sea of Okhotsk (Nishioka et al., 2007, 2013). Multiyear hydrographic observations along the A-line off the southeastern coast of Hokkaido have revealed a remarkable seasonal cycle in surface dFe that has a maximum value in winter, which is accompanied by deepening of the mixed-layer depth (MLD) (Nishioka et al., 2011). Observations have also shown that surface water in the Oyashio region in winter has a dFe/$NO_3$ ratio (0.036) that is substantially higher than in other HNLC regions. This is related to the influence of advection of Fe-rich water in the intermediate layer from the Sea of Okhotsk and to strong winter mixing, which reaches to the top of the intermediate water. The higher dFe/$NO_3$ ratio is caused by external Fe input from the shelf of the Sea of Okhotsk, and it is decoupled from the internal nutrient cycle. These results suggest that treatment of the dFe cycle is necessary when considering material cycles in the Oyashio region.

In the Oyashio region, remarkable decadal variability of phosphate ($PO_4$) has been reported based on long-term hydrographic data (Ono et al., 2001, 2002), and a modulating influence by 18.6-year tidal mixing in the Kuril Straits has been proposed (Tadokoro et al., 2009). In the Kuril Straits, subinertial, strong diurnal tidal currents generate both topographically trapped waves (Tanaka et al., 2010) and internal lee waves over shallow sills (Nakamura and Awaji, 2004), which lead to substantial vertical mixing. These tidal mixing processes have important roles in both the formation of low potential vorticity water for the North Pacific intermediate water (Talley, 1991) and the material circulations from the surface to deeper layers (Wong et al., 1998). Osafune and Yasuda (2006) argued that the decadal variation in intermediate-water properties in the Sea of Okhotsk is controlled by the formation rate of dense shelf water (DSW), which is influenced by the salinity flux attributable to tidally induced vertical mixing in the Kuril Straits (Nakamura et al., 2006). Therefore, the 18.6-year tidal mixing in the Kuril Straits also changes the nutrient flux at the surface, which leads to modification of nutrients in the downstream Oyashio region.

There is a possibility that climate change also has substantial impact on material transport in the Oyashio region on interannual–decadal timescales. Ito et al. (2004) investigated Oyashio transport in terms of the barotropic response to change of the wind-driven gyre circulation and found that year-to-year variability could be partly explained by the time-varying Sverdrup transport. Moreover, the coastal Oyashio, which is a coastally trapped barotropic current formed along the southeastern coast of Hokkaido in winter and spring (e.g., Kono et al., 2004), is also a possible cause of material transport. Nakanowatari and Ohshima (2014) highlighted that interannual variability of sea level near the Pacific coast of Hokkaido is controlled by arrested topographic waves (ATWs) induced by wind stress in the Sea of Okhotsk (Csanady, 1978). Yasunaka et al. (2016) examined the long-term variability of macronutrients in the subarctic North Pacific based on a newly developed nutrient dataset (1961–2012). They suggested that decadal fluctuation of surface nutrients in the subarctic North Pacific is influenced by deepening of the MLD and local advection related to large-scale atmospheric patterns such as the Pacific Decadal Oscillation (PDO). Similar to the physical mechanisms controlling macronutrients on interannual–decadal timescales, the influences of tidal mixing strength and climate change have been investigated based on statistical analyses of historical oceanographic observations. However, the effects of these influences on interannual–decadal variability of macronutrients in the Oyashio region have not yet been quantified.

Recently, using a regional ice–ocean model (Uchimoto et al., 2011, Nakanowatari et al., 2015) coupled with a biogeochemical model of $PO_4$ and dFe cycles (Parekh et al., 2005), Nakanowatari et al. (2017) reproduced the geographical and vertical distributions of surface $PO_4$ and dFe in the western subarctic North Pacific (i.e., an HNLC region). In this model, seasonal variation of dFe in the Oyashio region is simulated qualitatively, and its essential mechanism was found related to the southward western boundary current of the subarctic gyre and outflow from the Sea of Okhotsk, as well as to vertical entrainment, as reported by Nishioka et al. (2011). Their studies focused mainly on seasonal variation of dFe concentration in the Oyashio region, and thus the interannual variabilities of material cycles and their relation to climate change were not addressed. The satisfactory reproducibility of the climatological dFe and $PO_4$ distributions, and the implementation of the tidal mixing process in the Kuril Straits, motivated us to adopt this model for quantitative evaluation of the influence of 18.6-year tidal mixing and climate change on interannual–decadal variability of nutrients in the Oyashio region.

In this study, to evaluate the effects of climate change and 18.6-year tidal mixing on surface $PO_4$ in the Oyashio region on interannual–decadal timescales, we conducted hindcast and sensitivity experiments using an ice–ocean model coupled with a biogeochemical model, developed by Nakanowatari et al. (2017), with realistic atmospheric boundary conditions and 18.6-year tidal mixing fluctuations. On the interannual timescale, we focused on interannual variability of $PO_4$ in winter and evaluated the influence of wind-driven ocean current variability (i.e., Oyashio and coastal Oyashio variability). On the decadal timescale, we focused on the roles of climate change and 18.6-year tidal mixing fluctuations.

## 2. Data and methods

### 2.1. Model configuration

The physical–biogeochemical coupled model used in this study is based on a regional ocean general circulation model of the western subarctic North Pacific, which includes the Sea of Okhotsk (Uchimoto et al., 2011, 2014; Nakanowatari et al., 2015), coupled with a biogeochemical model with Fe cycles (Parekh et al., 2005). The physical model used in this study is based on the Center for Climate System Research Ocean Component Model (COCO ver. 3.4) coupled with a sea ice model (Hasumi, 2006). The ocean model solves the primitive-equation system under Boussinesq and hydrostatic approximations and uses a σ–z hybrid vertical coordinate with a free surface. The sea ice model is based on a two-category thickness representation, zero-layer thermodynamics (Semtner, 1976), and dynamics with elastic–viscous–plastic rheology (Hunke and Dukowicz, 1997). There are 51 levels in the vertical direction with thickness increasing progressively for the deeper layers (i.e., 27 layers from the surface to 500 m depth), the horizontal resolution is $0.5^\circ \times 0.5^\circ$, and the model domain covers the Sea of Okhotsk and the western subarctic gyre (Fig. 1a). In this model, the major components of the Kuril Straits such as the Bussol' Straits and Kruzenshtern Straits are represented, as shown in Fig. 1b.

To represent the effects of tidal mixing along the Kuril Straits, the increment of the vertical diffusivity coefficient ($K_z$) is applied artificially to the Kuril Straits (Fig. 1a) in accordance with the manner described by Uchimoto et al. (2014), where the maximum value of $K_z$ is at the bottom (500 $cm^2/s$) and it decreases gradually in shallower depths. This vertical profile of the parameterized $K_z$ reflects that diapycnal mixing processes are related to the breaking of internal lee waves (Nakamura and Awaji, 2004) and the dissipation of topographically trapped waves near sills (Tanaka et al., 2010). The lateral boundary conditions for temperature and salinity are based on monthly mean climatological values from the World Ocean Atlas 2001 (WOA2001) (Boyer et al., 2002; Stephens et al., 2002), and sea surface height (SSH) at the boundary is also restored to the climatological SSH obtained from the North Pacific model with the same configurations as our model. The settings of the numerical model scheme and parameters are identical to those of Uchimoto et al. (2014). This regional ocean general circulation model can successfully simulate the variations of wind-driven and thermohaline circulations on

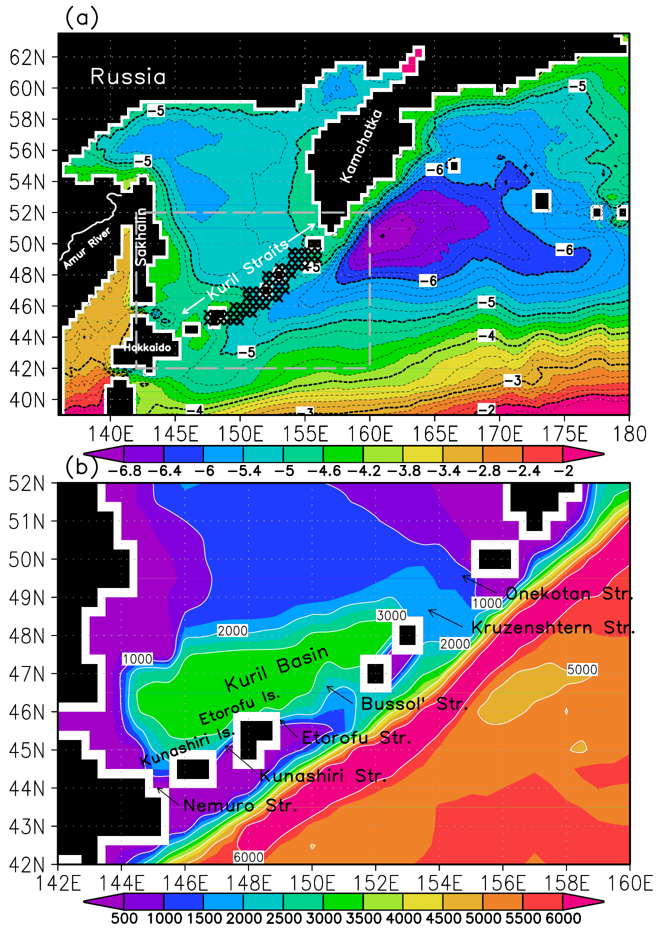


**Fig. 1.** (a) Model topography and climatological annual mean of dynamic height at the surface ($m^2/s^2$) in the model simulation during 1980–2010. Cross marks indicate where vertical diffusivity coefficients are enhanced. (b) Model topography around the Kuril Straits (rectangular region in panel a) and locations of individual straits.

seasonal–decadal timescales (Matsuda et al., 2009; Uchimoto et al., 2011; Nakanowatari et al., 2015).

The biogeochemical model includes $PO_4$, dissolved organic phosphate (DOP), and dFe cycles (Parekh et al., 2005). In the euphotic zone, $PO_4$ and DOP are governed by advection and diffusion terms, with source/sink terms related to biological uptake and remineralization. Biological uptake of $PO_4$ is formulated by Michaelis–Menten kinetics with dFe, $PO_4$, and light limitations. The Fe cycle is governed by advection and diffusion terms, with source/sink terms related to biological uptake and external source terms related to the sediment flux of the northwestern shelf in the Sea of Okhotsk and atmospheric dust flux. In this model, atmospheric dust flux at the sea surface occurs in the sea ice region; therefore, dust accumulated on sea ice (i.e., dFe flux) was ignored in this study. Using this ocean general circulation model coupled with a biogeochemical model that includes the Fe cycle forced by two major sources (i.e., atmospheric dust and the sediment in the northwestern shelf), Uchimoto et al. (2014) successfully simulated the spatial distribution of dFe concentration in the intermediate water in and around the Sea of Okhotsk.

In this study, we used the biogeochemical model parameters, i.e., half-saturation constant for dFe and sediment flux value, adopted by Nakanowatari et al. (2017) to reproduce realistic distributions of $PO_4$ and dFe (i.e., HNLC region) in the western subarctic North Pacific. Moreover, we also adopted a modified irradiance condition that indirectly expresses the vertical movement of phytoplankton due to MLD deepening in winter (Nakanowatari et al., 2017). A brief description of the biogeochemical model including these modifications is given in Appendix A.

Generally, nitrate is used as the limiting macronutrient in the model of the subarctic North Pacific ecosystem (e.g., Kawamiya et al., 2000), which requires implementation of complex processes of nitrogen fixation and denitrification. This study focused primarily on the roles of the physical processes in the Sea of Okhotsk (i.e., wind-driven coastally trapped current, sea ice formation, and tidal mixing). Thus, based on the assumption that $PO_4$ behaves in a manner similar to nitrate with a constant Redfield ratio, $PO_4$ was used as the limiting macronutrient in this model. This approximation appears valid in our model domain (i.e., the western subarctic North Pacific) because background levels of $PO_4$ and nitrate are not depleted before the dFe is exhausted.

Furthermore, our model constituted a simple nutrient-type biogeochemical model in which the numbers of phytoplankton were not predicted explicitly; thus, phytoplankton growth and mortality were assumed balanced. Consequently, in the bloom season, the rate and duration of $PO_4$ uptake in the coastal region appear underestimated and overlong, respectively, owing to the simple formulation adopted for the uptake rate in this model. Nonetheless, as biological uptake is likely to be small in winter, this simple model enabled us to examine the mechanism responsible for the timing of the wintertime increase in $PO_4$ in the Oyashio region.

The lateral boundary conditions for $PO_4$ were restored to the monthly mean values obtained from the World Ocean Atlas 2009 (WOA09) (Garcia et al., 2010) in a manner similar to temperature and salinity. The lateral boundary conditions of dFe were fixed as constants based on observational values (Takata, 2005; Takata et al., 2008; Nishioka et al., 2007, 2013) and the results of a biogeochemical model simulation (Misumi et al., 2011).

Surface meteorological parameters were derived from daily mean global atmospheric reanalysis products (ERA-Interim), from the European Centre for Medium-Range Weather Forecasts, with 0.75° resolution in both latitude and longitude from 1979 to 2010 (Dee et al., 2011). Turbulent and latent heat fluxes were computed using bulk formulas of these meteorological components, e.g., 2-m temperature, 2-m dewpoint temperature, and absolute 10-m wind speed (Kara et al., 2000). Radiation fluxes were given as the sum of net solar and longwave radiation fluxes. Fresh water fluxes were adopted as evaporation minus total precipitation derived from ERA-Interim products, but river runoff data were fixed to the monthly climatology of observed river discharge (Dai and Trenberth, 2002). Wind stress data were derived from surface flux outputs of ERA-Interim products.

Eolian dust flux data were derived from a monthly mean dust deposition dataset from 1979 to 2010 (Luo et al., 2003). This dataset was produced from the MATCH chemistry transport model coupled with the DEAD desert entrainment and deposition model driven by NCEP-NCAR reanalysis data. We applied the dFe flux at the sea surface based on the assumption that Fe constituted 3.5 wt% of the total dust (wet and dry depositions) and that it dissolved instantaneously at the sea surface with solubility of 1%. The validity of this assumption has been demonstrated by earlier numerical simulations focusing on the distribution of dFe at intermediate depth (Uchimoto et al., 2014) and in the surface layer (Nakanowatari et al., 2017).

To account for the influence of the 18.6-year lunar nodal cycle on tidal mixing along the Kuril Straits, we artificially applied time-dependent vertical diffusivity coefficients ($K_z'(t)$) of temperature, salinity, and biogeochemical tracers to the Kuril Straits, as follows:

$$K_Z'(t) = K_Z + K_Z \times \alpha cos(2\pi(t-1969)/18.6), \quad (1)$$

where $\alpha$ is the nodal modulation factor for all lunar constituents. In this study, we set this factor at 0.2, which leads to 20% fluctuation in the strength of tracer mixing across the 18.6-year period. The fraction of the 18.6-year period is determined by the fact that the nodal modulation factor of the principal diurnal constituent $K_1$ is ±19% (Pugh, 1987). The data sources for the boundary conditions used in this study are summarized in Table 1.

### 2.2. Hindcast experiment

The design of the hindcast experiment was as follows. Initially, the ice–ocean coupled model was integrated for 50 years from initial conditions based on the climatological temperature and salinity of WOA2001, under surface atmospheric forcing based on daily mean climatological ERA Interim data. Based on the physical conditions of the final year of spin-up and the climatological $PO_4$ of WOA2009, the coupled physical–biogeochemical model was integrated for 27 years under the same atmospheric forcing that included eolian dust flux data. After completion of the spin-up experiment using the coupled physical–biogeochemical model, the hindcast experiment was performed using historical atmospheric forcing, eolian dust flux, and 18.6-year tidal mixing modulation from 1979 to 2010. Analysis of the hindcast experiment is based on the results from 1980 to 2010 owing to the problem of initial shock in 1979.

To evaluate the contributions of atmospheric boundary forcing and tidal mixing strength to the decadal fluctuation of $PO_4$ in the Oyashio region, we additionally performed three perturbation experiments (Table 2). In addition to these factors, we also examined the influence of eolian dust flux on the decadal variability of $PO_4$ in the Oyashio region because there is a possibility that the interannual variability of surface dFe flux indirectly affects surface $PO_4$. In the perturbation experiments, interannual fluctuations were restricted to atmospheric boundary forcing (ATM), tidal mixing strength (TIDE), and eolian dust flux (DUST); the other factors were fixed at monthly mean climatological values from 1979 to 2010, and the tidal mixing strength was fixed to a constant value in both the ATM and the DUST experiments.

### 2.3. Observational data

This study evaluated the climatological features and interannual variability of the simulated $PO_4$ including physical variables (temperature and salinity) in the Oyashio region. To achieve this, we prepared a new gridded dataset based on in situ oceanographic observations (1965–2008) archived by the World Ocean Database 2013 (WOD13) (Boyer et al., 2013), and repeated A-line cross sections for long-term monitoring of physical and biochemical parameters in the Oyashio region and the Kuroshio–Oyashio confluence (1990–2010) obtained by the Hokkaido and Tohoku National Fisheries Research Institutes of the Japan Fisheries Research and Education Agency (Fig. 2). The A-line observations were obtained approximately 5 times per year, including January and March. It should be noted that the nutrient samples during 2009–2010 were derived only from A-line monitoring data.

The monthly mean climatologies of $PO_4$ and the physical variables were calculated at standard depth levels for each $0.5^\circ \times 0.5^\circ$ grid box using a simple distance-weighted method (Levitus and Boyer, 1994). For the distance-weighted function, we used weighted averaging with a Gaussian window with a half-width of 150 km and an e-folding scale of 75 km. If fewer than five observations were within the window, the box was regarded as having no data. For examination of the interannual variability of $PO_4$ and the physical variables, the monthly mean anomalies were calculated as the raw value minus the corresponding monthly mean climatology, and the calculated anomalies were gridded using simple averaging in a monthly $0.5^\circ \times 0.5^\circ$ grid box.

To diagnostically examine the dynamical response of the simulated current field and its relation to the large-scale atmospheric pattern, we used North Pacific ERA-Interim monthly mean sea level pressure (SLP) and wind stress data (Dee et al., 2011) to examine the large-scale atmospheric pattern related to the variability of the simulated $PO_4$. These atmospheric data were also used for calculation of the alongshore volume transport of the ATW and the Sverdrup transport in the Oyashio region (see Section 4).

To evaluate the interannual variability of the simulated coastal Oyashio and first branch of Oyashio current in winter, we used monthly mean tide-gauge sea level data at Kushiro station (42°58′N, 144°22′E, see Fig. 2) derived as part of the Permanent Service for Mean Sea Level (Woodworth, 1991). The tide-gauge sea level data reflect the dynamical displacement of sea level related to the geostrophic current on the continental shelf in winter (Itoh and Ohshima, 2000, Isoda et al., 2003, Nakanowatari and Ohshima, 2014), and also the interannual variability of the western boundary current of the subarctic gyre, i.e., the first branch of the Oyashio (Isoguchi and Kawamura, 2006). As the tide-gauge data at Kushiro station show a remarkable trend of increase, we removed this linear trend from the time series.

**Table 1**
Physical and biogeochemical conditions applied to the hindcast experiment.

| Interannual variational forcing | Sources | Period |
|---|---|---|
| Atmospheric flux | ERA-Interim (Dee et al., 2011) | Jan 1979 to Dec 2010 |
| Dust deposition flux | Wet and dry dust flux estimated from NCEP–NCAR reanalysis (Luo et al., 2003) | – |
| 18.6-year cycle in tidal mixing strength | 20% of $K_z$ in the Kuril Straits | – |

**Table 2**
List of perturbation experiments.

| Experiment | Wind stress and turbulent heat fluxes | 18.6-year tidal mixing strength | Atmospheric dust flux |
|---|---|---|---|
| ATM | Interannual change | Constant | Seasonal cycle |
| TIDE | Seasonal cycle | Interannual change | Seasonal cycle |
| DUST | Seasonal cycle | Constant | Interannual change |

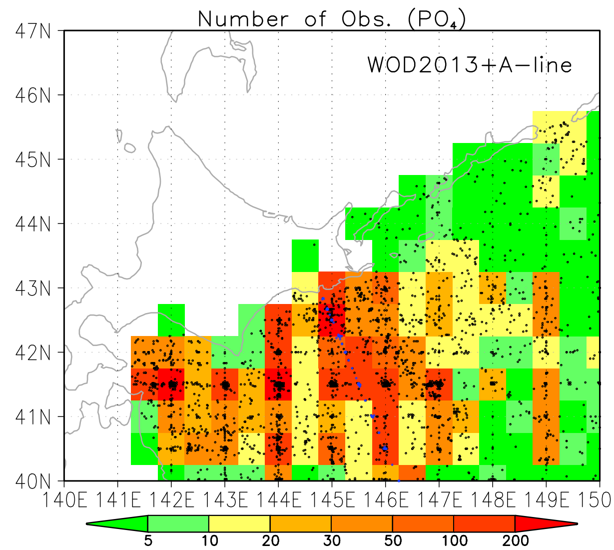


**Fig. 2.** Spatial distribution of the $PO_4$ profiles from WOD13 (black dots) and A-line (blue dots) from 1965 to 2010. The total number of observations at the surface are represented by colored shading. The purple triangle indicates the location of the tide gauge at Kushiro station.

### 2.4. Statistical analysis

In this study, we conducted correlation and regression analyses of the simulated data and the representative $PO_4$ time series in the Oyashio region to diagnostically examine the physical mechanisms controlling $PO_4$ variability. On the decadal timescale, we applied a low-pass filter to the simulated and observed data to extract the decadal signal, and we adopted a nonparametric method based on a Monte Carlo simulation, using a phase-randomization technique that generated 1000 surrogate time series (Kaplan and Glass, 1995), to estimate the significance of the correlation.

## 3. Simulated surface water properties and $PO_4$ in the Oyashio region

To evaluate the representation of the Oyashio water mass in a mean state, we examined the ocean temperature at 100-m depth, where the Oyashio water is defined by temperature of <5 °C (Yoshida, 1992; Kono and Kawasaki, 1997). The wintertime (DJF) climatology of observed ocean temperature at 100-m depth in the area offshore of Hokkaido is shown in Fig. 3. Two branches of cold-water mass (<5°C) are evident along the steep slope of the Kuril–Kamchatka trench (approximately 6000-m depth) and the offshore area. These two minima are consistent with the first and second branches of the Oyashio current (Kuroda et al., 2019). The climatological distribution of $PO_4$ at the surface in winter, when surface nutrient concentration is maximum, is shown in Fig. 3b. In association with the cold-water masses of the first and second branches of the Oyashio current, two areas of reasonably high $PO_4$ values (>2 μM) can be seen in the region offshore of Etorofu Island (Fig. 3b).

In the simulated data, the southwestward intrusion of the cold-water mass (<5°C) along the steep slope (i.e., the first branch of the Oyashio current) is represented qualitatively, whereas the offshore component (i.e., the second branch of the Oyashio current) is obscure (Fig. 3c). The simulated $PO_4$ values are also reasonably high along the Kuril–Kamchatka trench, but the two local maxima of observed $PO_4$ are not simulated well (Fig. 3d). The deficiency regarding the two branches of the Oyashio current in our model might be related to inadequate spatial resolution. The resolution of our model of approximately 50 km is too coarse to resolve the mesoscale current system. Therefore, we focused on the $PO_4$ variability in the first branch of the Oyashio current (OY1), which is defined by the rectangular region (42°–43°N, 145°–148°E).

The seasonal cycle of simulated $PO_4$ in the Oyashio region is evaluated using area-averaged data. A time series of observed monthly mean $PO_4$ in the mixed layer, averaged over the OY1 region, is shown in Fig. 4. In this area, the seasonal cycle of $PO_4$ is characterized by a peak (approximately 1.6 μM) in February–March and a trough (0.4 μM) in June–October, which is consistent with earlier studies (Harrison et al., 1999; Saito et al., 2002). This seasonal cycle of observed $PO_4$ is

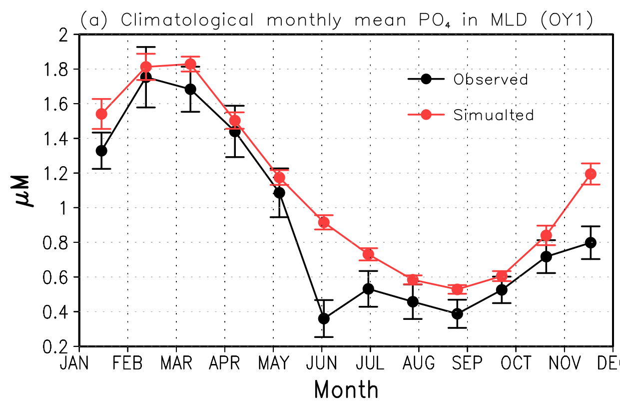


**Fig. 4.** Time series of climatological monthly mean $PO_4$ (μM) in the mixed layer averaged over the OY1 region for observed (black) and simulated (red) data. Error bars indicate standard deviations of monthly mean $PO_4$ in the mixed layer from 1979 to 2010.

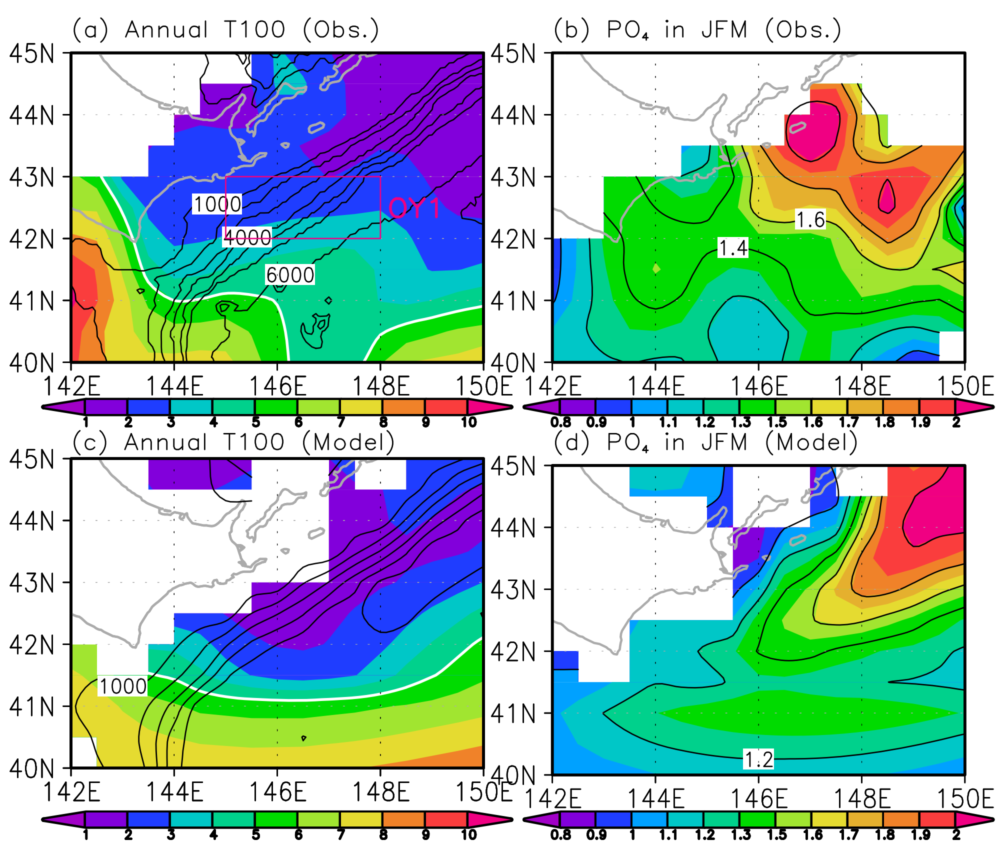


**Fig. 3.** Spatial distribution of (a, c) ocean temperature (°C) at 100-m depth and (b, d) $PO_4$ (μM) at the surface in January – March (JFM) in observed and simulated data. In the left-hand panels, the boundary of 5 °C is shown by the white contour and seafloor depth > 1000 m is shown by the black contours. The bathymetry data for the observations were derived from ETOPO5. The location of region OY1 (42°–43°N, 145°–148°E) is shown by the magenta rectangle in panel a.

simulated qualitatively by our model, although the simulated $PO_4$ is somewhat overestimated (by 0.2 μM) throughout the entire year. The standard deviation of monthly mean $PO_4$ in the observed data shows seasonal dependency with a maximum value in winter and a minimum value in summer. The model data also show similar seasonal dependency of interannual variability, although the simulated fluctuation is underestimated by approximately 50% throughout the entire year. Thus, the model data qualitatively represent the seasonal cycle of $PO_4$ variability and the seasonal dependency of the interannual variability in the Oyashio region.

To evaluate the representation of interannual variability of the first branch of Oyashio water, we examined the annual mean sea surface salinity in the Oyashio region. Time series of annual observed and simulated sea surface salinity (SSS), averaged over the OY1 region, are shown in Fig. 5a. Although the year-to-year variability of simulated SSS is relatively weak, the multiyear variability including decadal-scale variability is simulated qualitatively. The correlation between them is 0.43, which is significant at the 95% confidence level. Although our model resolution is not that fine, the interannual variability of the first branch of the Oyashio current is simulated qualitatively. For examination of the interannual variability of the coastal Oyashio and the first branch of the Oyashio current in winter, we compared the sea level at Kushiro station in winter (January–March) with the corresponding sea level on the continental shelf of Hokkaido (43°N, 145.5°E) in the model. The correlation between the time series of monthly simulated and observed sea level in winter (January–March) is 0.48 (significant at the 95% confidence level). Time series of tide-gauge sea level at Kushiro station and simulated SSH, shown in Fig. 5b, are comparable on the interannual timescale, although the amplitude of the simulated sea level is relatively underestimated. This result suggests that the interannual variability of the coastal Oyashio and/or the Oyashio current, at least the wintertime barotropic component, is simulated qualitatively by the model.

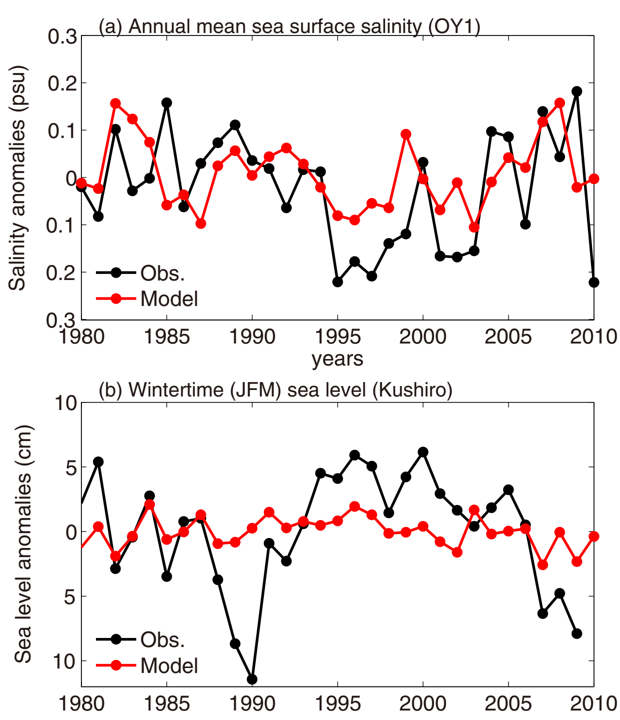


**Fig. 5.** (a) Time series of annual mean sea surface salinity anomalies averaged over the OY1 region for observed (black) and simulated (red) data. (b) Time series of wintertime (JFM) tide-gauge sea level anomalies at Kushiro station and simulated sea level anomalies over the Pacific-side continental shelf of Hokkaido (43°N, 145.5°E).

## 4. Results

### 4.1. Interannual variability in winter

Cross-correlation analysis of observed and simulated monthly mean $PO_4$ shows that the simulated $PO_4$ in January and February is correlated significantly with the observed $PO_4$ in March, but that there is no significant correlation between simulated and observed $PO_4$ variability in March (Table 3). The insignificant correlation in March is partly caused by inadequate representation of the baroclinic component of the coastal Oyashio in our model attributable to model resolution (Sakamoto et al., 2010), because intrusion of the coastal Oyashio water mass enhances $PO_4$ supply in late winter. Nevertheless, the barotropic response of the coastal current and western subarctic gyre driven by wind stress is reproduced qualitatively, even by this intermediate-resolution model, as discussed in Section 3. Therefore, at least the role of the barotropic response of the coastal trapped current system and the subarctic gyre circulation could be evaluated in this study. The simulated $PO_4$ in January is almost identical to that in February (i.e., the correlation between them is 0.94); therefore, the model output for January was considered representative of winter in the following analysis.

A time series of observed $PO_4$ anomalies in March is shown in Fig. 6. The observed $PO_4$ anomalies show remarkable year-to-year variability throughout the analyzed period. The temporal variations of the simulated $PO_4$ anomalies in January also show year-to-year variability similar to that of the observed data, although the amplitude of the simulated $PO_4$ anomalies is somewhat lower than that of the observed $PO_4$ anomalies. It is noteworthy that the simulated $PO_4$ is also correlated significantly with dFe in January ($r = 0.83$). As the correlation between the time series of interannual variability of dFe at the surface and local atmospheric dust flux is small ($r = -0.54$), atmospheric dust flux is considered inessential for reproducing the interannual variability of dFe in the Oyashio region in the model.

To clarify the mechanism of interannual variability of surface $PO_4$ in January, we performed a budget analysis of $PO_4$ in the mixed layer. In this analysis, we evaluated each term in the $PO_4$ tendency equation integrated over the mixed layer, as follows:

$$\frac{1}{MLD}\frac{\partial}{\partial t}\left(\int_{MLD} PO_4 dz\right) = ADV + MIX + BIO + residuals,$$

$$ADV = \frac{1}{MLD}\int_{MLD}\{-\nabla\cdot(\vec{v}PO_4) + K_H\nabla_h^2 PO_4\}dz, \tag{2}$$

$$MIX = \frac{1}{MLD}\int_{MLD}\frac{\partial}{\partial z}\left(K_V\frac{\partial PO_4}{\partial z}\right)dz + \frac{1}{MLD}\frac{dMLD}{dt}PO_4(MLD)$$

where ADV indicates the $PO_4$ flux convergence attributable to ocean currents and lateral mixing due to subgrid-scale eddies, MIX indicates the vertical mixing attributed to both buoyant and mechanical mixing, and BIO indicates the source/sink term arising from photosynthesis uptake and organism degradation. Note that the first term on the right-hand side in the expression for ADV includes both mean and eddy components when averaged temporally. The MLD is determined based

**Table 3**
Correlations between observed and simulated monthly $PO_4$ time series in the OY1 region during 1979–2010.

| | | Observation | | | |
|---|---|---|---|---|---|
| | | Dec (N = 3) | Jan (N = 18) | Feb (N = 15) | Mar (N = 17) |
| Model | Dec | – | 0.21 | 0.37 | 0.36 |
| | Jan | – | 0.23 | 0.31 | **0.56** |
| | Feb | – | 0.20 | 0.22 | **0.58** |
| | Mar | – | −0.05 | 0.01 | −0.03 |

Parentheses indicate the degree of freedom for the observed time series.
Values in bold indicate correlation coefficient significant at the 95% confidence level.

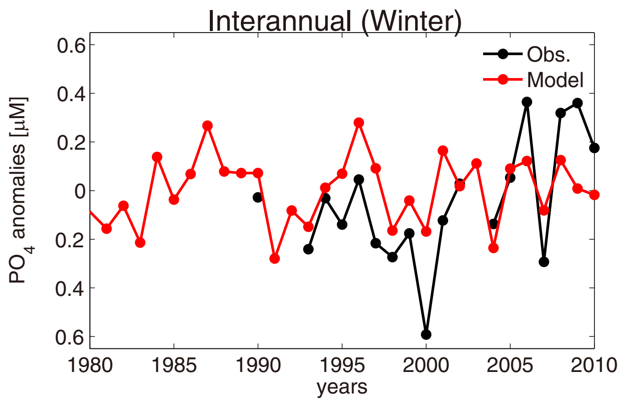


**Fig. 6.** Time series of observed $PO_4$ anomalies (black) in the mixed layer in March and simulated $PO_4$ anomalies (red) in the mixed layer in January from 1980 to 2010 averaged over the OY1 region.

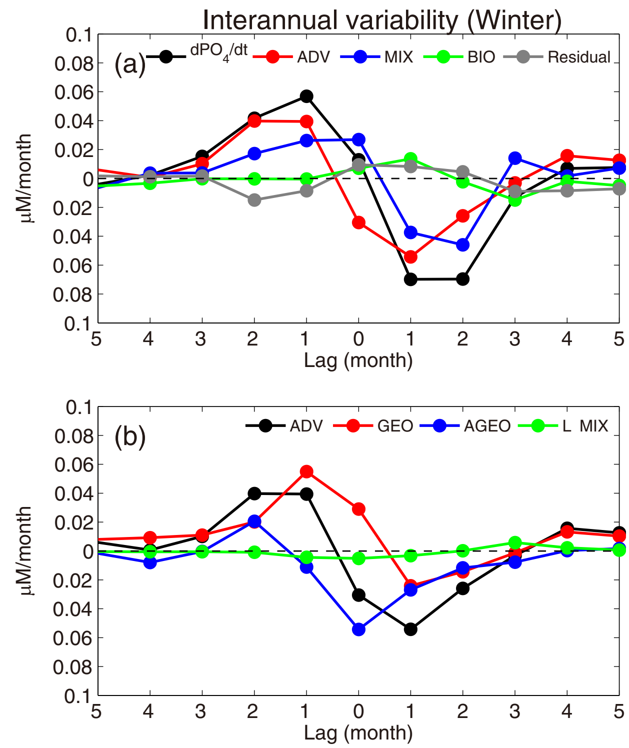


**Fig. 7.** (a) Lead–lag regression coefficients of monthly mean $PO_4$ budget terms ($PO_4$ tendency, ADV, MIX, BIO, and residuals) in Eq. (2) averaged over the OY1 region on the time series of normalized MLD-$PO_4$ anomaly in January. A negative value of lag (month) means that the $PO_4$ budget term leads the normalized MLD-$PO_4$ anomaly. (b) Same as panel a but for the geostrophic current, ageostrophic current, and lateral mixing terms in Eq. (3).

on the potential density criterion of 0.125 in $\sigma_\theta$ unit. It is noted that the tendency term of $PO_4$ related to MLD change is included as the second term in the expression for MIX. The residual term arises from the temporal and vertical finite difference expressions.

To identify the principal budget term responsible for the interannual variability of surface $PO_4$ in January, we first calculated the monthly mean budget terms averaged over the OY1 region, which include all timescales longer than one month. Then, we imposed the lead–lag regression coefficients of these budget terms onto the time series of normalized $PO_4$ anomalies in the mixed layer averaged over OY1 in January (hereafter, called MLD-$PO_4$), which allowed extraction of the main term and month contributing to the interannual variability. The lead–lag regression coefficients for the $PO_4$ tendency term show a maximum value of 0.05 μM/month in December, which leads MLD-$PO_4$ by one month (Fig. 7a). In December (one-month lead time), the lateral advection term makes a large contribution to the MLD-$PO_4$ budget, although vertical mixing is not negligible. At this lead time, the biological and residual terms are small in comparison with the physical terms. Therefore, it is concluded that the lateral advection process in December controls the interannual variability of MLD-$PO_4$ in the model.

For further clarification of the physical process responsible for the lateral advection term, we divided it into three terms: the geostrophic current, ageostrophic current such as Ekman transport and upwelling, and subgrid-scale mixing, which can be expressed as follows:

$$ADV \simeq -\underbrace{\vec{v}_g grad_h PO_4}_{geostrophic\ current} - \underbrace{\left(\vec{v}_a grad_h PO_4 + w_a \frac{\partial PO_4}{\partial z}\right)}_{ageostrophic\ current} + \underbrace{K_H \nabla_h^2 PO_4}_{lateral\ mixing} \quad (3)$$

where $v_g$ and $v_a$ represent the geostrophic and ageostrophic components of the ocean currents, respectively. The ageostrophic current speed was obtained by subtracting the geostrophic current speed from the total current speed at each depth, where the former includes both baroclinic and barotropic components and is derived from the SSH and temperature–salinity profiles in the model. The lead–lag regression coefficients of these components on the normalized MLD-$PO_4$ demonstrate that the geostrophic current term controls the ADV term in December (Fig. 7b).

To clarify the physical mechanism related to the ADV term in December, we examined the spatial distribution of the simulated geostrophic current and SSH field in December. The interannual signal related to the ADV term in December was extracted by the lag regression analysis based on the normalized time series of MLD-$PO_4$ in the Oyashio region in January. A regression map of the 1-month leading geostrophic current vectors on the time series of MLD-$PO_4$ anomaly in January is shown in Fig. 8a. We found a southwestward geostrophic current anomaly in the Oyashio region, which seems to be extended from the east coast of Sakhalin Island. As $PO_4$-rich water forms along the Kuril Straits owing to tidally induced vertical mixing throughout the year (Fig. 8a), lateral advection of surface $PO_4$ is likely to be explained by the combination of the anomalous southwestward geostrophic current and high-$PO_4$ water in the Kuril Straits. The regression map of the 1-month leading SSH on MLD-$PO_4$ in January shows a positive (negative) anomaly in the coastal (offshore) region (Fig. 8b). These results indicate that the southwestward geostrophic current anomaly in the Oyashio region is controlled by SSH variability in both coastal and offshore regions.

We examined the contribution of the coastal Oyashio and the Oyashio current to the interannual variability of the southwestward geostrophic current in the Oyashio region. The vertical cross section of the simulated geostrophic current speed in December at 43°N shows that the coastal Oyashio is simulated qualitatively as a mostly barotropic current at around 147°E (Fig. 9a). The surface current speed for the shallow depth region is 5 cm/s, which is half that of the observed value in December (Kusaka et al., 2009). For the Oyashio current, the southward current axis is found at around 149°E with speed of 2 cm/s, which is less than the annual mean baroclinic current speed (10 cm/s) estimated based on long-term hydrographic observations (Kuroda et al., 2017). Thus, although the model underestimates the speed for the coastal Oyashio and Oyashio current, both current systems can be distinguished.

Vertical profiles of the regression coefficients of 1-month leading southward geostrophic current at 43°N indicate that the geostrophic current anomaly that is responsible for the $PO_4$ anomaly in the Oyashio region is confined to the shelf region with depth of <100 m and the deeper layer (Fig. 9a), which corresponds to a reasonably large SSH gradient from 146.5°–148.5°E (Fig. 9b). This result indicates that the southward current anomaly is caused by both the coastal Oyashio and the Oyashio current. In the following, we diagnostically evaluate the

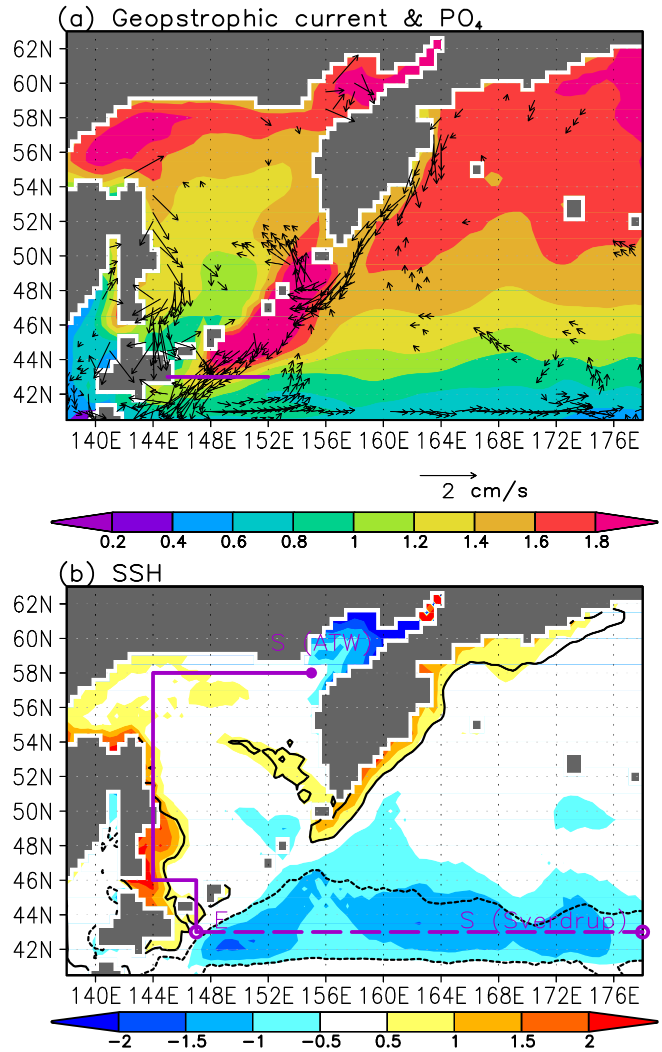


**Fig. 8.** (a) Regression map of 1-month leading (December) geostrophic current speed (cm/s, vectors) in the mixed layer on the time series of normalized MLD-$PO_4$ in January. In panel a, the climatological $PO_4$ in the mixed layer in December is also shown. Vectors for which the correlations are significant at the 95% confidence level are shown. The statistical significance for the vectors was estimated based on the absolute value. (b) Same as panel a but for SSH (cm, colors) in December. The solid and dashed contours indicate regions where the positive and negative correlation between them is significant at the 95% confidence level, respectively. The integral routes for ATW transport and Sverdrup transport in the OY1 region are shown by solid and dashed purple lines, respectively.

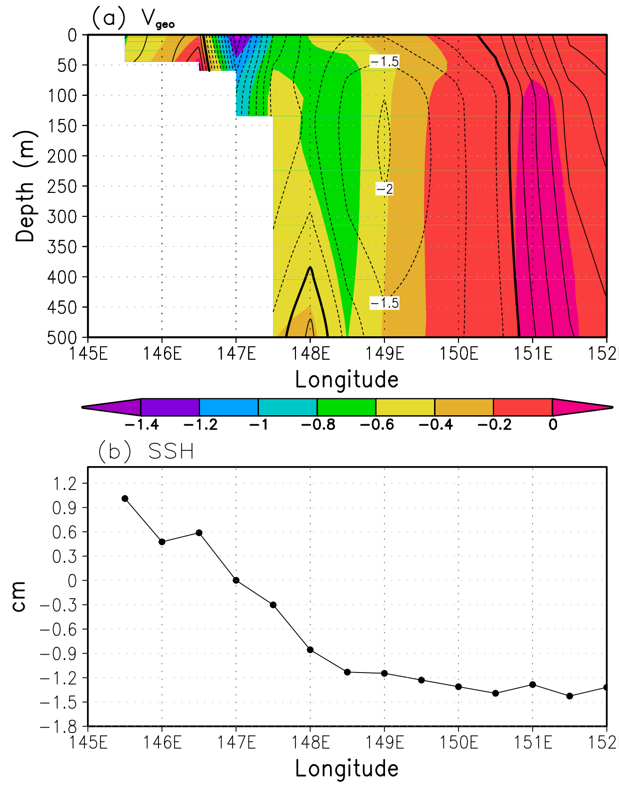


**Fig. 9.** (a) Vertical cross section (43°N) of the regression coefficients (colors) for 1-month leading (December) meridional geostrophic current speed (cm/s) on the time series of normalized MLD-$PO_4$ in January. Negative value means southward. In panel a, the climatological geostrophic current speed in December is also shown by black contours (contour interval: 0.5 cm/s). (b) Same as Fig. 8b but for the longitudinal cross section for the regression coefficients of SSH (cm) in December at 43°N from the east coast of Hokkaido.

influence of these wind-driven currents on the interannual variability of the southwestward geostrophic current in the Oyashio region based on ATW and Sverdrup transport theory.

According to Csanady (1978), the alongshore volume transport of an ATW at OY1 ($V_{ATW}$) can be derived using the following equation:

$$V_{ATW} = \int \frac{\tau_l}{\rho f} dl, \tag{4}$$

where $\tau_l$ is the alongshore component of wind stress, $\rho$ is the density of water, and $f$ is the Coriolis parameter. This equation means that $V_{ATW}$ at OY1 is the sum of the Ekman transport integrated along the integral route. According to an earlier study (Nakanowatari and Ohshima, 2014) and the extent of the positive anomaly in the regression map of SSH in December (Fig. 8b), we determined that the integral route for $V_{ATW}$ starts from the west of the Shelikhov Gulf (Fig. 8b).

The time-varying Sverdrup transport at OY1 ($V_s$) can be calculated using the following equation:

$$V_S = -\frac{1}{\beta\rho} \int curl\overrightarrow{\tau} dx, \tag{5}$$

where $\beta$ is the y-derivative of the Coriolis parameter and $\overrightarrow{\tau}$ is a wind stress vector. The integral route is defined by the latitudinal line from the eastern model boundary (180°W) to the OY1 region (Fig. 8b). Although we ignored the effect of wind stress in the eastern North Pacific, it appears negligible because barotropic Rossby waves are largely blocked by the Emperor Seamounts located at around 170°E and thus its signal is damped in the Oyashio region (Nakanowatari et al., 2015, Kuroda et al., 2017).

Time series of the ATW transport and the southward geostrophic current in December are shown in Fig. 10a. The time series are strongly correlated on the interannual timescale throughout the entire period. The correlation between them is 0.65, which is significant at the 95% confidence level, and accounts for 42% of the total variance of the geostrophic current in January. The southward geostrophic current in December is also correlated significantly with the Sverdrup transport (r = 0.55), but the correlation coefficient is somewhat smaller than that for ATW transport (Fig. 10b).

Finally, we examine the large-scale atmospheric circulation patterns responsible for ATW and Sverdrup transport in the Oyashio region. A regression map of wind stress vector and SLP in December on the time series of normalized simulated MLD-$PO_4$ in January is presented in Fig. 11. In the Sea of Okhotsk, the northerly wind stress anomaly is prominent, which is related to the pressure gradient between the anomalous Aleutian Low (AL) and the Siberian High (SH), which is a typical SLP pattern of the wintertime monsoon. The correlation

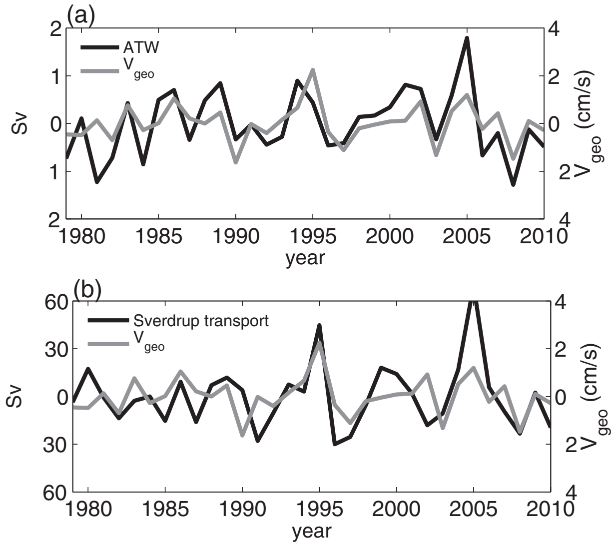


**Fig. 10.** Time series of (a) the monthly mean ATW and (b) Sverdrup transport anomalies (Sv, black) and the meridional component of geostrophic current speed anomalies (cm/s, gray) in the OY1 region in December. The sign of Sverdrup transport is inverted (i.e., a negative value means southward). The scale for the geostrophic current speed is shown on the right-hand side.

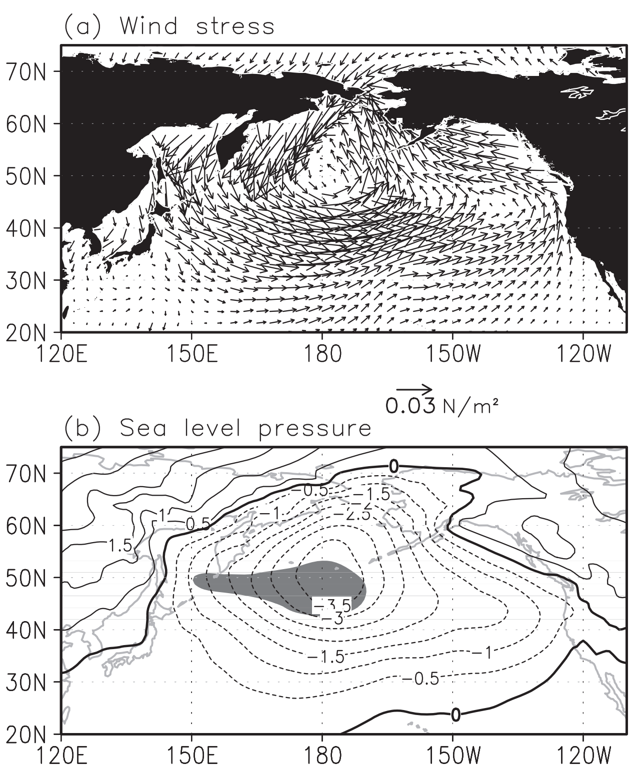


**Fig. 11.** Regression maps of 1-month leading (December) wind stress ($N/m^2$, vectors) and (b) sea level pressure (hPa, contours) on the time series of normalized MLD-$PO_4$ in January. In panel b, light (dark) shading indicates the region where the positive (negative) correlation is significant at the 95% confidence level.

coefficients between the time series of the simulated MLD-$PO_4$ anomaly in January and the 1-month leading SLPs for the AL (48°N, 180°W) and the difference between the AL and SH (AL − SH) are − 0.54 and 0.57, respectively, which are statistically significant at the 95% confidence level (Table 4). These results indicate that the AL–SH pressure gradient is conducive to the generation of ATW transport. We also examined the correlation between the simulated MLD-$PO_4$ and the North Pacific Index (NPI) (Trenberth and Hurrell, 1994) and the PDO index (PDOI) (Mantua et al., 1997). Although the correlations of the NPI and PDOI with the simulated MLD-$PO_4$ are relatively large, they are statistically insignificant (Table 4).

**Table 4**
Correlations between simulated MLD-$PO_4$ in January and climate indices (NPI, PDOI) in December, the AL (SLP at 48°N, 180°W), SH (SLP at 55°N, 125°E), and their difference (SH − AL) in December.

| | AL | SH | SH–AL | NPI | PDOI |
|---|---|---|---|---|---|
| Correlations | **−0.54** | 0.44 | **0.57** | −0.46 | 0.39 |

Values in bold indicate correlation coefficient significant at the 95% confidence level.

### 4.2. Decadal variability

To extract the decadal component from the surface $PO_4$ variability, we applied a 7-year low-pass filter to the observed and simulated data before conducting statistical analysis. A time series of the annual mean MLD-$PO_4$ anomaly calculated from observed data is shown in Fig. 12. The low-pass-filtered time series (>7 years) shows significant decadal variability with positive (negative) anomalies in 1980, 1995, and 2005 (1970, 1990, and 2000). These positive and negative phases of decadal fluctuation are almost consistent with the results of an earlier study (Tadokoro et al., 2009). The model qualitatively simulates decadal fluctuations similar to the observed anomalies since the 1980s, although the phase of the decadal component is somewhat lagged (i.e., by 2 years). The lead–lag correlation analysis between the time series of observed and simulated $PO_4$ anomaly with a low-pass filter indicates that the maximum correlation ($r = 0.67$, significant at the 95% confidence level) is obtained when the latter time series is advanced by 2 years.

Time series of the 7-year low-pass-filtered annual mean MLD-$PO_4$ anomalies in OY1 for the perturbation experiments are shown in Fig. 13. Overall, the decadal variability of annual mean MLD-$PO_4$ in the hindcast experiment can be explained well by ATM, i.e., the correlation between them is 0.78, which is significant at the 95% confidence level. The correlation between the annual mean MLD-$PO_4$ in TIDE and the hindcast experiment is rather low ($r = 0.21$), but the annual mean MLD-$PO_4$ in TIDE shows substantial fluctuations with positive anomalies in the late 1980s and 2000s and a negative anomaly in the late 1990s. These positive and negative anomalies are almost consistent with the strong and weak phases of the 18.6-year lunar nodal cycle. In particular, the

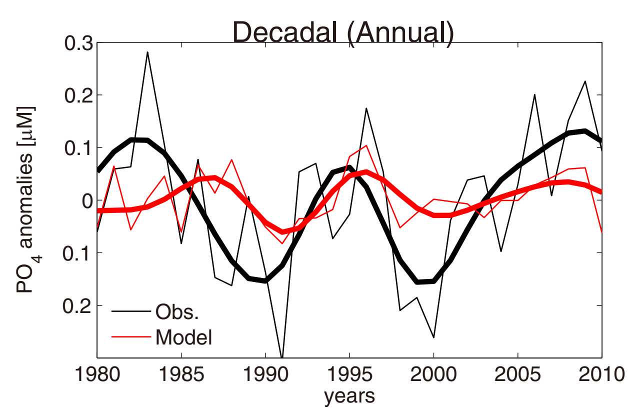


**Fig. 12.** Time series of the annual mean of observed and simulated $PO_4$ (μM) anomalies in the mixed layer averaged over the OY1 region. The 7-year low-pass-filtered values for the observed and simulated $PO_4$ time series are shown by bold lines.

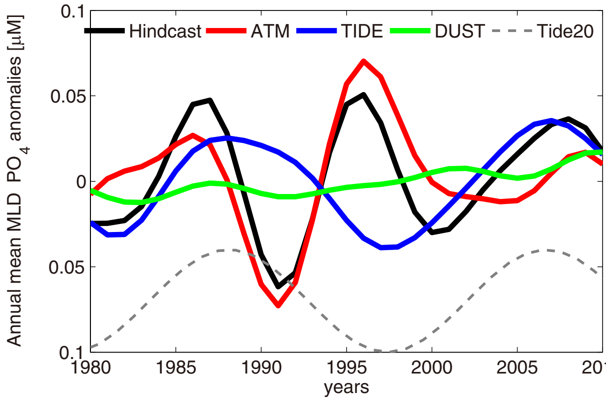


**Fig. 13.** Time series of 7-year low-pass-filtered annual mean MLD-$PO_4$ anomalies (μM) for the hindcast experiment (black), ATM (red), TIDE (blue), and DUST (green) for the OY1 region. The sinusoidal curve for 18.6-year tidal mixing strength is shown by dashed gray line.

difference in the annual mean MLD-$PO_4$ anomaly between the hindcast and ATM experiments is relatively large during the strong phase of tidal mixing strength. These results indicate that the decadal variability of MLD-$PO_4$ is mostly explained by atmospheric wind forcing, but that the influence of the 18.6-year tidal mixing strength is not negligible.

The decadal variability of the annual mean MLD-$PO_4$ anomaly in the DUST experiment is weakly correlated with that in the hindcast experiment ($r = 0.35$), but the variance is rather small. We also examined the correlation relationship between the decadal variability of annual mean dFe and $PO_4$ in the mixed layer in the hindcast experiment. The correlation between the time series of annual mean MLD-$PO_4$ and dFe with a 7-year low-pass filter is 0.46, which is statistically insignificant. Therefore, the mechanism controlling the decadal variability of annual mean $PO_4$ in the Oyashio region is considered not influenced by biological processes through the availability of dFe.

The physical processes responsible for the decadal variability of annual mean $PO_4$ in the ATM experiment was examined using a budget analysis for the decadal component (>7 year) of the annual mean MLD-$PO_4$ based on Eqs. (2) and (3). To evaluate the contribution of each term in the $PO_4$ budget, we performed lead–lag regression analysis on the time series of the annual mean MLD-$PO_4$ anomaly in ATM. The maximum regression coefficient of the tendency in annual mean MLD-$PO_4$ is when the tendency term leads the annual mean MLD-$PO_4$ by 2–3 years. The regression coefficient of the 2-year leading tendency term is comparable with that of the ADV term, while those for MIX, BIO, and the residual terms are negligible or of the opposite sign (Fig. 14a). Examination of the contributions of the geostrophic current, ageostrophic current, and lateral mixing terms on the ADV term show that the geostrophic current term is responsible for the ADV (Fig. 14b).

To clarify the physical mechanism of the geostrophic current term, we examined the decadal component of the geostrophic current speed and surface $PO_4$ anomaly in the model. A regression map of the 2-year leading annual mean $PO_4$ anomaly and geostrophic current in ML on the time series of annual mean MLD-$PO_4$ with a 7-year low-pass filter is presented in Fig. 15. Significant positive correlation for the 2-year leading annual mean $PO_4$ field is found in the upstream region of OY1. However, there is no meaningful signal on the southwestward Oyashio strength and the coastal Oyashio. This result indicates that the mean Oyashio current flowing down the gradient around the area of anomalously high $PO_4$ causes geostrophic $PO_4$ flux into the Oyashio region.

The above analysis raises questions regarding the source of the decadal signal in the region upstream of OY1. As Oyashio water is highly influenced by outflow water from the Sea of Okhotsk, it is possible that the decadal $PO_4$ signal originates in the Sea of Okhotsk. To clarify the source of the decadal $PO_4$ signal, we examined the temporal evolution of

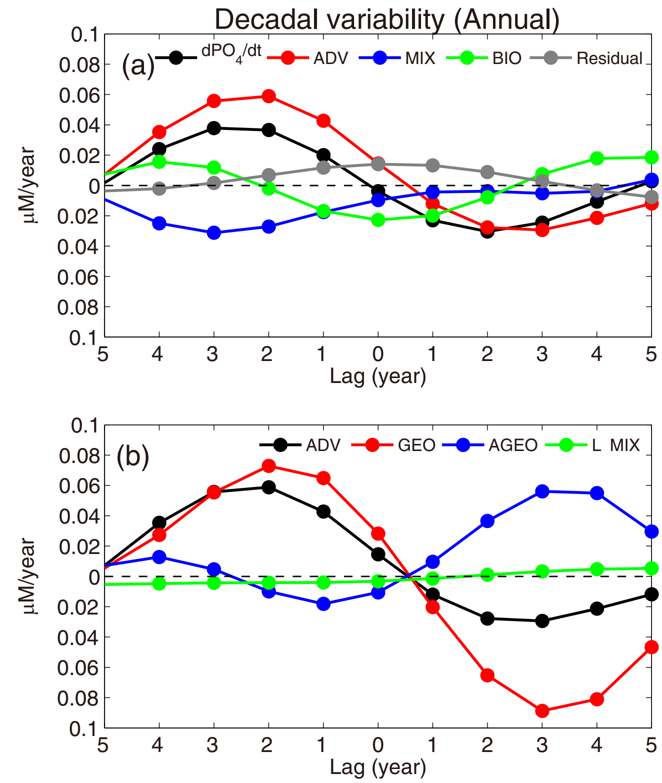


**Fig. 14.** (a) Lead–lag regression coefficients of 7-year low-pass-filtered annual mean $PO_4$ budget terms ($PO_4$ tendency, ADV, MIX, BIO, and residuals) in Eq. (2) averaged over the OY1 region on the time series of the normalized annual mean MLD-$PO_4$ anomaly. A negative value of lag (year) means that the $PO_4$ budget term leads the normalized MLD-$PO_4$ anomaly. (b) Same as panel a but for the geostrophic current, ageostrophic current, and lateral mixing terms in Eq. (3).

decadal variability of annual mean $PO_4$ in the Sea of Okhotsk through lead–lag correlation analysis. Fig. 16 shows the vertical cross section of the temporal evolution of the decadal anomaly in annual mean $PO_4$ along the pathway of the East Sakhalin Current (ESC) (Fig. 15). We found that the decadal signal could be traced back to the northwestern shelf (NWS), with a lead time of 6 years along the ESC at the depth of 100–250 m (Fig. 16a). As the depth of this water mass corresponds to that of the isopycnal layer at 26.6–26.8 $\sigma_\theta$, the decadal signal lies along the water mass between the winter mixed layer (100 m) (Ohshima et al., 2005) and the intermediate water (heavier than 26.8$\sigma_\theta$) (Gradyshev et al., 2003). Significant positive correlation appears in the Kuril Basin at a lag of −4 years (Fig. 16d), indicating that the decadal variability of annual mean $PO_4$ on the NWS takes approximately 2 years to reach the Kuril Basin, a distance of approximately 1000–1500 km (Fig. 16d). Considering that the annually averaged speed of the ESC in this model is approximately 2 cm/s, the time lag of 2 years between the $PO_4$ on the NWS and in the Oyashio region is consistent with advection time of the mean current speed in the model. Significant positive correlation is still found in the Kuril Basin at a lag of −2 years relative to the time series of annual mean MLD-$PO_4$ (Fig. 16f). As the mean current is very weak in the Kuril Basin, the persistence of the significant correlation for approximately 2 years is related to residence time in the Kuril Basin. With no lag, significant positive correlation is found in the Oyashio region and in/around the Kuril Straits (Fig. 16h), indicating that the decadal signal in the subsurface layer emerges at the surface owing to tidally induced vertical mixing.

As the decadal signal of $PO_4$ is confined to the bottom of the NWS (Fig. 16a and 16b), wind-driven upwelling would be a likely source of the decadal variability of $PO_4$ on the NWS via input of high-$PO_4$ water

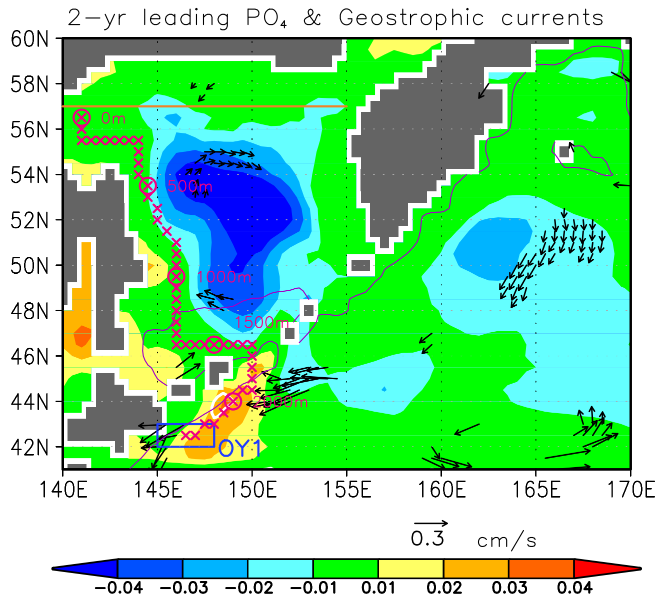


**Fig. 15.** Regression map of 2-year leading annual mean $PO_4$ (μM, colors) and geostrophic current (cm/s, vectors) in the mixed layer on the time series of normalized annual mean MLD-$PO_4$ with 7-year low-pass filter for ATM. Contour indicates the region where the correlation between them is significant at the 95% confidence level. Vectors for which the correlations are significant at the 95% confidence level are shown. The statistical significance for the vectors was estimated based on the absolute value. The locations of the vertical cross sections in Figs. 16 and 17 are shown by magenta and orange lines, respectively.

from the deep layer. Thus, we examined upwelling of $PO_4$ water on the NWS, the relation between the upwelling and the surface wind, and the cause of the decadal variability of the upwelling. A vertical cross section of the regression coefficient of 7-year leading annual mean $PO_4$ on the NWS (57°N) on the time series of annual mean MLD-$PO_4$ with a low-pass filter is presented in Fig. 17. A meaningful positive anomaly of annual mean $PO_4$ is confined near the bottom of the NWS, which is accompanied with an upward current velocity anomaly of $0.02 \times 10^{-3}$ cm/s (Fig. 17b). As relatively high-$PO_4$ water (>3.0 μM) is found near the shelf region in the mean state, the significant positive anomaly of annual mean $PO_4$ is likely induced by upward flux of $PO_4$-rich water from the deep layer. It is noted that there is no meaningful signal on the western side of the NWS where DSW forms in winter. Therefore, the decadal variability of subsurface $PO_4$ is unrelated to the formation process of DSW.

We evaluated the influence of Ekman upwelling on vertical velocity on the NWS using ERA-Interim wind stress curl data. In this analysis, we examined four seasonal Ekman upwelling velocities from winter (DJF) to autumn (SON) and their relation to the time series of annual mean MLD-$PO_4$. From the lead–lag correlation analysis, we determined that annual mean MLD-$PO_4$ is correlated significantly with 8-year leading DJF Ekman upwelling velocity on the NWS (Fig. 18). The Ekman upwelling velocity anomaly on the NWS is 0.02–0.04 $\times 10^{-3}$ cm/s, which is comparable with the upward velocity anomaly at around 150°E (Fig. 17b).

To understand the wintertime atmospheric circulation patterns related to Ekman upwelling in the Sea of Okhotsk, we performed regression analyses of wind stress curl and SLP on annual mean MLD-$PO_4$. A regression map of 8-year leading wind stress curl over the North Pacific in DJF on annual mean MLD-$PO_4$ Is shown in Fig. 19. A positive anomaly of wind stress curl is evident over the Sea of Okhotsk and subarctic North Pacific. The regression map of SLP indicates that the positive anomaly of wind stress curl is related to deepening of the AL, which is accompanied with positive anomalies in the subtropical North Pacific (Fig. 19b). This dipole pattern of SLP regression resembles the positive phase of the West Pacific (WP) pattern or North Pacific oscillation, which is the second mode of SLP in the North Pacific (Linkin and Nigam, 2008).

We thus calculated the correlations between annual mean MLD-$PO_4$ and the WP index derived from the Climate Prediction Center (Barnston and Livezey, 1987). We also examined the statistical relationship between annual mean MLD-$PO_4$ and the NPI, which is the major decadal climate index of the North Pacific. We obtained significant positive correlation between the time series of annual mean MLD-$PO_4$ and the WP index with a 7-year low-pass filter ($r = 0.71$, significant at the 90% confidence level) when the latter leads the former by 8 years. However, the correlation between the wintertime NPI and the time series of annual mean MLD-$PO_4$ is weak ($r = 0.18$) when the former leads the latter by 8 years. Thus, the decadal variability of surface $PO_4$ in the Oyashio region is strongly linked to the wind-stress curl related to the WP pattern.

## 5. Discussion and conclusions

In this study, we investigated the principal mechanisms controlling interannual–decadal variations in surface $PO_4$ concentrations in the Oyashio region and their relationships to climate change using a regional ice–ocean coupled model with a simple biogeochemical cycle. The model qualitatively simulates interannual–decadal variations of surface $PO_4$, including the realistic seasonal cycle of surface $PO_4$ with a maximum value (1.5 μM) in winter. Interannual variability of surface $PO_4$ in the Oyashio region is prominent in winter. The correlation between the time series of hindcast and observed $PO_4$ anomalies in winter is 0.56, which is significant at the 95% confidence level. Budget analysis of $PO_4$ in the mixed layer indicates that lateral advection contributes most to interannual variability of $PO_4$ and that vertical mixing is a secondary contributor. This result is consistent with the fact that the seasonal variation of dFe in the Oyashio region is controlled by lateral advection and vertical mixing processes, as shown by earlier study (Nakanowatari et al., 2017), indicating that the wind-driven current system is also crucial on the interannual timescales.

Theoretical analysis on the wind-driven current revealed that the geostrophic current related to the coastal Oyashio is well explained by ATW transport in the Sea of Okhotsk and by Sverdrup transport in the North Pacific. The atmospheric pattern conducive to these wind-driven ocean currents is deepening of the AL and strengthening of the SH, which is a typical atmospheric pattern of the wintertime monsoon. Although large-scale atmospheric change and the resultant ocean current in the North Pacific is shown to be a major factor of macronutrient transport in the subarctic North Pacific, including the Oyashio region (Yasunaka et al., 2016), the importance of the coastal trapped current in the Sea of Okhotsk to the process of feeding surface macronutrients into the Oyashio region is a new finding by this study.

The role of coastal Oyashio water in late winter on $PO_4$ variability could not be addressed in this study because of insufficient representation of $PO_4$ variability in March in the model. The Oyashio region is also highly influenced by northward intrusion of mesoscale warm eddies separated from the Kuroshio Extension area (Itoh and Yasuda, 2010), which are also not represented in our model owing to the model domain and grid size. These mesoscale currents, including the second branch of the Oyashio, are likely to influence the advection time of water from the Kuril Straits through the diverted advection route. Therefore, it is possible that the time lag of 1–2 months between the simulated and observed $PO_4$ in winter is attributable to the lack of mesoscale currents in our model. For clarification of the importance of these mesoscale currents to the transport pathway of nutrients in the Oyashio region, a further numerical modeling study based on a high-resolution biogeochemical model is needed.

On the decadal timescale, the hindcast experiment also shows realistic decadal variability of annual mean $PO_4$ in the Oyashio region, which is characterized by significant quasidecadal fluctuations with positive (negative) peaks in 1985, 1995, and 2005 (1990 and 2000). The

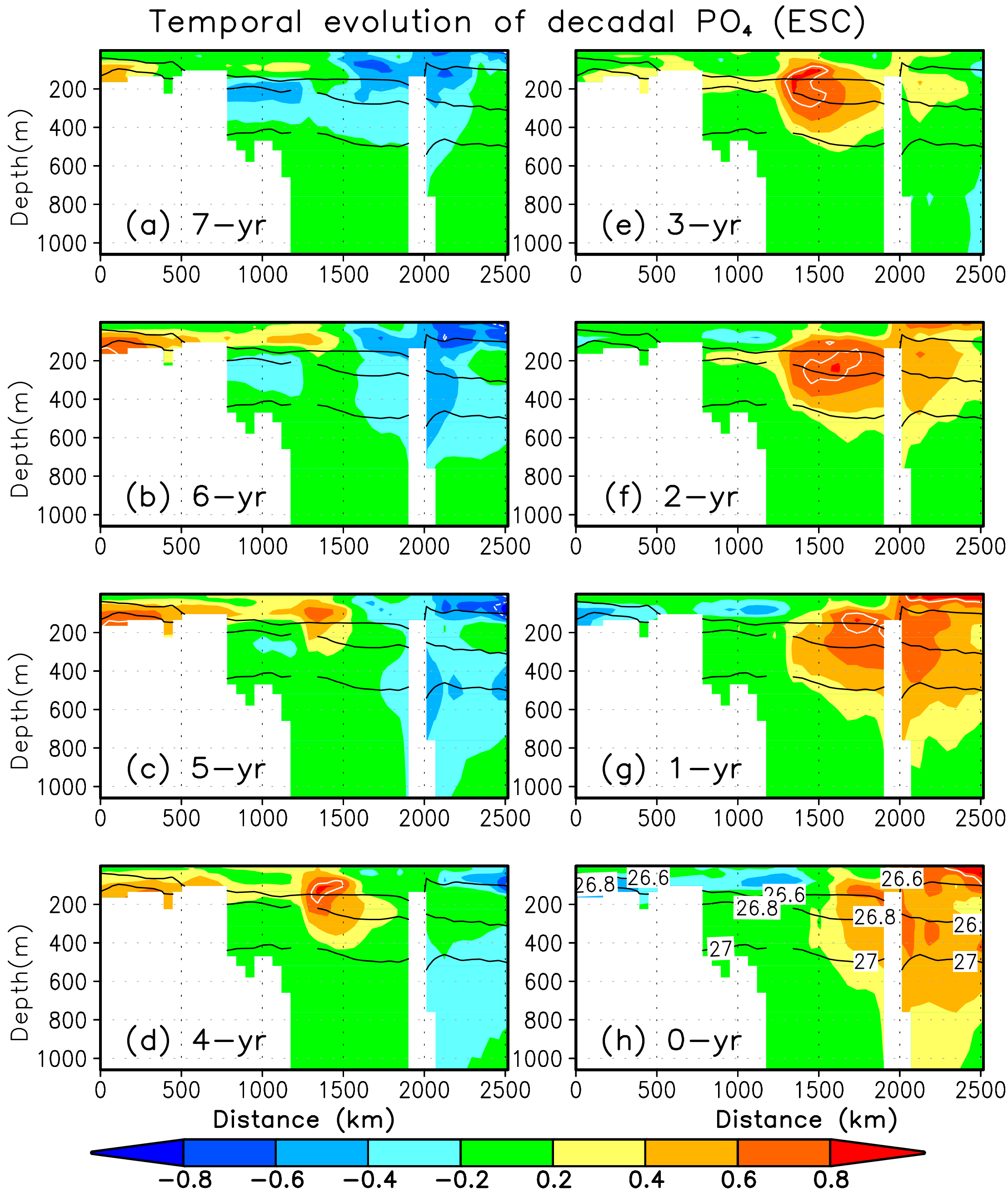


**Fig. 16.** Lag correlation map of annual mean $PO_4$ along the pathway of the ESC (shown in Fig. 15) from the surface to 1000-m depth with time series of annual mean MLD-$PO_4$ with 7-year low-pass filter for ATM at the lead time of (a) +7, (b) +6, (c) +5, (d) +4, (e) +3, (f) +2, (g) +1, and (h) 0 years. The white contours indicate the region where the correlation between them is significant at the 95% confidence level. Climatological potential density is shown by black contours. The geographical location for the distance from the NWS is shown in Fig. 15.

sensitivity experiments demonstrate that decadal variability of annual mean $PO_4$ in the Oyashio region is explained primarily by atmospheric wind conditions, with changes in tidal mixing having a secondary role. Budget analysis of $PO_4$ in the mixed layer indicates that $PO_4$ is predominantly controlled by lateral advection and that local vertical mixing is negligible on the decadal timescale. Diagnostic analysis of the sensitivity experiment data in ATM shows that decadal variability of $PO_4$ is advected from the NWS in the Sea of Okhotsk along the ESC through the subsurface layer. The decadal signal of $PO_4$ on the NWS reaches the Kuril Basin after 4 years and remains within the Kuril Basin for an additional 2 years. The decadal signal of subsurface $PO_4$ in the Kuril Basin upwells to the surface via the tidally induced vertical mixing process in and around the Kuril Straits, and is advected downstream by the southwestward mean Oyashio current. These results imply that wind-driven upwelling in the Sea of Okhotsk is crucial for the decadal variability of surface $PO_4$ in the Oyashio region.

Although sea ice production and the resultant formation of dense shelf water in the NWS region is known as an essential process of Fe (i.e., micronutrient) transport in the North Pacific (e.g., Nishioka et al., 2011), our results differ from those of earlier studies. In particular, we found that the WP teleconnection pattern, which is one of the primary modes of low-frequency variability during boreal winter, leads the surface $PO_4$ variability in the Oyashio region by several years. This finding is important regarding long-term prediction of the biogeochemical system and further implications for the fishery resources in the Oyashio region.

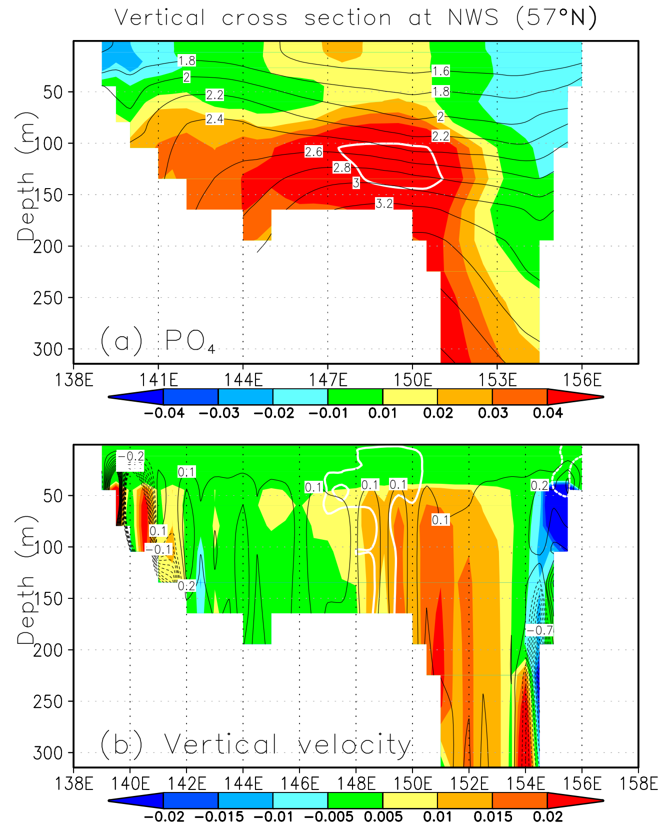


**Fig. 17.** Regression map of 7-year leading annual mean (a) $PO_4$ (μM, colors) and (b) vertical velocity ($\times 10^{-3}$ cm/s, colors) along the NWS (57°N) on time series of normalized annual mean MLD-$PO_4$ with 7-year low-pass filter for ATM. The white contour indicates the region where the correlation between them is significant at the 95% confidence level. In each panel, climatological values of annual mean $PO_4$ and vertical velocity are shown by black contours. In panel b, the contour interval for the climatological value is $0.1 \times 10^{-3}$ and absolute values $> 1.0 \times 10^{-3}$ are not shown. The geographical location for the distance from the NWS is shown in Fig. 15.

We note that our model has some biases regarding the physical and biogeochemical parameters. The advection time of the decadal component of $PO_4$ variability from the NWS to the Kuril Basin is estimated to be 2–4 years in our model simulation. Mensah et al. (2019) reported that the DSW signal at the subsurface layer can reach the Kuril Basin in half a year. Conversely, based on a historical hydrographic dataset of the past several decades, Uehara et al. (2014) showed that interannual variability of intermediate water temperature in the Kuril Basin is correlated significantly with 2-year leading DSW salinity. As the spatial resolution of our ocean model is not fine, overestimation of the advection time in our model is likely related to underestimation of ESC velocity. In fact, the southward speed of the ESC in our model is approximately 10–15 cm/s in January, which is slower than the observed velocity (20–30 cm/s) obtained from mooring measurements (Mizuta et al., 2003). The underestimation of ESC velocity is consistent with our result indicating that the simulated $PO_4$ value in the Oyashio region lags the observed value by 1 year. Moreover, the simulated variability of $PO_4$ is underestimated in comparison with observed data owing to inadequate configurations and settings for both physical and biogeochemical models. Therefore, research involving full ecosystem modeling using a high-resolution ocean model is needed for further quantitative examination of the effects of climate change on the nutrient condition and primary production in the studied region, which is left for future work.

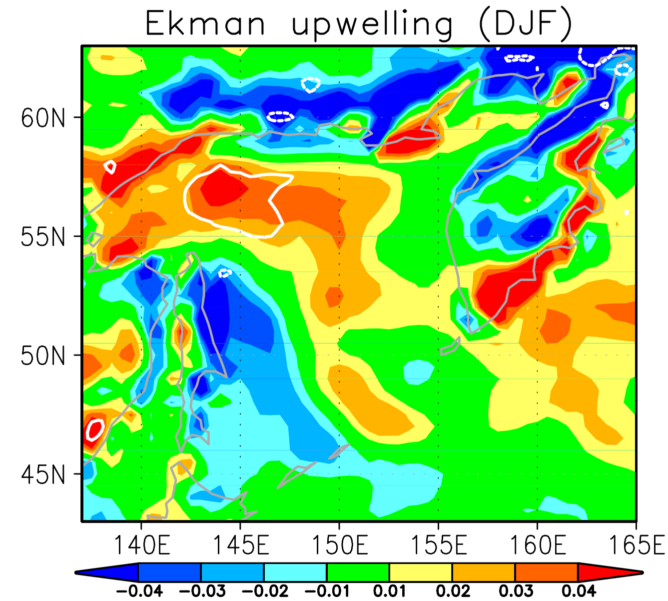


**Fig. 18.** Regression map of 8-year leading wintertime (DJF) mean Ekman upwelling ($10^{-3}$ cm/s, colors) on time series of normalized annual mean MLD-$PO_4$ with 7-year low-pass filter for ATM. The white contour indicates the region where the correlation between the Ekman upwelling and the time series of MLD-$PO_4$ is significant at the 95% confidence level.

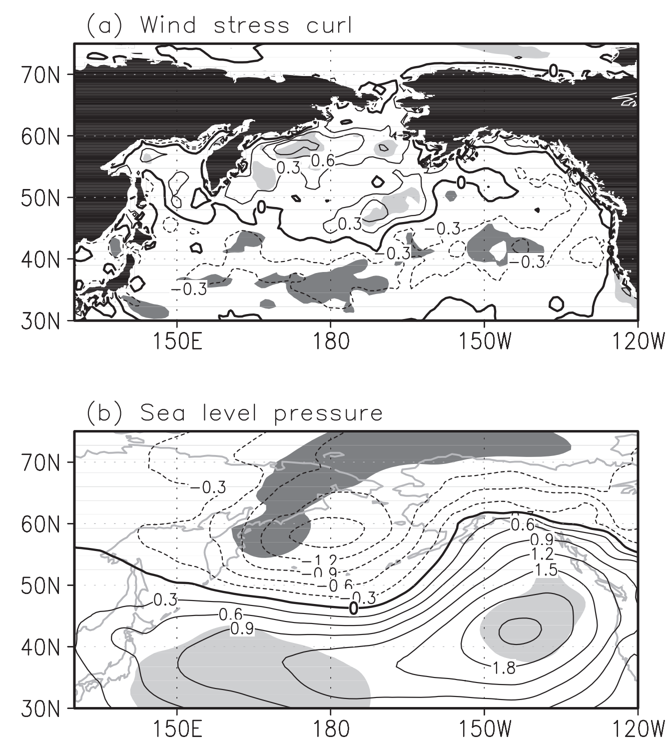


**Fig. 19.** Regression map of 8-year leading (a) wind stress curl ($\times 10^{-7}$N/m$^3$, contours) and (b) sea level pressure (hPa, contours) in winter (DJF) on time series of normalized annual mean MLD-$PO_4$ with 7-year low-pass filter for ATM. Light (dark) shading indicates the region where the positive (negative) correlation between them is significant at the 95% confidence level.

**Declaration of Competing Interest**

The authors declare that they have no known competing financial interests or personal relationships that could have appeared to influence the work reported in this paper.

## Acknowledgments

We thank N. Mahowald for providing the dust dataset (1979–2010). Phosphate data in the Oyashio region were obtained from the A-line monitoring database of the Japan Fisheries Research and Education Agency (http://tnfri.fra.affrc.go.jp/seika/a-line/a-line_index.html). Numerical calculations were performed using the HITACHI SR16000 at the high-performance computing system of Hokkaido University and the SGI UV1000 at the Pan-Okhotsk Information System of Hokkaido University. We wish to thank the two anonymous reviewers and the editor for their fruitful constructive comments. A number of figures were produced using the GrADS package developed by B. Doty. This work was supported by JSPS KAKENHI [grant numbers 16K21586, 16H01585, 26247076, 17KK0014, 17H01156, and 18H04909], Joint Usage/Research Center for Interdisciplinary Large-scale Information Infrastructures (JHPCN), the Arctic Challenge for Sustainability (ArCS) project of the Ministry of Education, Culture, Sports, Science, and Technology of Japan, the Grant for Joint Research Program of the Institute of Low Temperature Science, Hokkaido University, Japan (21G026), and the Environment Research and Technology Development Fund (JPMEERF20214002) of the Environmental Restoration and Conservation Agency of Japan. We thank James Buxton MSc from Edanz Group (https://en-author-services.edanzgroup.com/) for editing a draft of this manuscript.

## Appendix A. Biogeochemical model

The biogeochemical model used in this study solves three state variables: phosphate ($PO_4$), dissolve organic phosphate (DOP), and dissolved Fe (dFe). The concentrations of $PO_4$ and DOP are governed by advection and diffusion terms, with source/sink terms related to biological uptake and remineralization processes, as follows:

$$\begin{aligned}\frac{\partial PO_4}{\partial t} &= Adv + Diff + \lambda PO_4 + \begin{cases} -\Gamma \\ -\dfrac{\partial F(z)}{\partial z}(below\ euphotic\ zone)\end{cases}, \\ \frac{\partial DOP}{\partial t} &= Adv + Diff - \lambda DOP + \begin{cases} \nu\Gamma \\ 0(below\ euphotic\ zone)\end{cases},\end{aligned} \tag{A1}$$

where $\Gamma$ represents biological uptake of $PO_4$. Eq. (A1) means that part of the $PO_4$ biologically uptaken in the euphotic layer ($\nu\Gamma$) enters the DOP pool at the same grid point. The residual ($(1-\nu)\Gamma$) in the euphotic layer is exported as particulates to the aphotic layer, which can be expressed in the form of the power law of Martin et al. (1987), i.e., ($F(z) = \int_{h_e}^{0}(1-\nu)\Gamma dz(z/h_e)^{-b}$), and the remineralization is expressed as the convergence of the flux. DOP is continuously remineralized with an e-folding scale ($\lambda$) of 6 months in both euphotic and aphotic layers.

Biological uptake of $PO_4$ ($\Gamma$) is formulated using Michaelis–Menten kinetics with Fe, $PO_4$, and light limitations, as follows:

$$\Gamma = \alpha\frac{PO_4}{PO_4 + K_{PO_4}}\frac{Fe}{Fe + K_{Fe}}\frac{I}{I + K_I}, \tag{A2}$$

where $\alpha$ is the maximum export rate, and $K_{PO_4}$, $K_{Fe}$, and $K_I$ represent half-saturation constants for $PO_4$, Fe, and light, respectively. $K_I$ is set to 30 $W/m^2$, which is identical to the original version of Parekh et al. (2005). Here, we set $K_{PO_4}$, $K_{Fe}$, and $\alpha$ to 0.5 μM, 0.12 nM, and 1.0, respectively, according Uchimoto et al. (2014).

Daily mean shortwave radiation flux data are applied as irradiance ($I_0$), which decays exponentially from the sea surface downward with an e-folding scale ($h_e$), as follows:

$$I = I_0 e^{-\frac{z}{h_e}}. \tag{A3}$$

In this study, $h_e$ is 10.86 m, which makes irradiance at 50 m (i.e., the bottom of the euphotic layer) approximately 1% of that at the sea surface. In sea ice regions, the decay of irradiance attributable to sea ice is estimated as a function of albedo, ice thickness, and decay scale in ice (Perovich, 1998).

To express indirectly the migration of phytoplankton, we artificially mixed irradiance strength in the mixed layer as follows:

$$I' = \frac{1}{h_{MLD}}\int_{h_{MLD}}^{0} I dz, \tag{A4}$$

where $h_{MLD}$ is the mixed-layer depth (MLD), which is determined by the density change from the ocean surface of $0.125\sigma_\theta$.

The dFe concentration is governed by advection and diffusion terms, with source/sink terms related to biological uptake and external source/sink terms, as follows:

$$\frac{\partial dFe}{\partial t} = Adv + Diff + \lambda DOPR_{Fe} + \underbrace{S_{Fe} + J_{Fe} + Sed_{Fe}}_{External\ Source/Sink} + \begin{cases} -\Gamma R_{Fe} \\ \dfrac{\partial dF(z)}{\partial z}R_{Fe}(below\ euphotic\ zone)\end{cases} \tag{A5}$$

The biological uptake, export, and remineralization terms are proportional to those in the phosphate equations with the proportionality coefficient of $R_{dFe}$, which is proportional coefficient of the dFe:P ratio (Parekh et al., 2005). The dFe is assumed to be the sum of the free dFe' and complexed dFeL forms, where L represents ligands.

In this model, the free form of Fe ($Fe'$) is assumed susceptible to scavenging by the formulation of $J_{Fe} = -\tau k_0 C_p^{\phi} Fe'$, where $C_p$ is the particulate concentration calculated by $F(z) = C_p W_{sink}$, and $Fe'$ is controlled by an equilibrium relationship: $K_{FeL}L = [FeL]/[Fe'][L']$. The values of the scavenging rate ($k_0$), export coefficient ($\phi$), scavenging scaling factor ($\tau$), ligand conditional stability coefficient ($K_{FeL}$), and particulate sinking rate ($W_{sink}$) are identical to those proposed by Parekh et al. (2005). The total ligand (i.e., the sum of FeL and L') is set at 1.2 nM in accordance with earlier studies (Misumi et al., 2011; Uchimoto et al., 2014).

## References


Barnston, A.G., Livezey, R.E., 1987. Classification, seasonality and persistence of low-frequency atmospheric circulation patterns. Mon. Weather Rev. 115, 1083–1126.

Boyer, T.P., Stephens, C., Antonov, J.I., Conkright, M.E., Locarnini, R.A., O'Brien, T.D., Garcia, H.E., 2002. World Ocean Atlas 2001: Salinity. In: NOAA Atlas NESDIS 50, vol. 1, U.S. Government Printing Office, Washington, D.C, pp. 176.

Boyer, T.P., Antonov, J.I., Baranova, O.K., Garcia, H.E., Johnson, D.R., Mishonov, A.V., O'Brien, T.D., Seidov, D., Smolyar, I., Zweng, M.M., Paver, C.R., Locarnini, R.A., Reagan, J.R., Coleman, C., Grodsky, A., Levitus, S., National Oceanographic Data, C., Ocean Climate, L., 2013. World Ocean Database 2013.

Chiba, S., Ono, T., Tadokoro, K., Midorikawa, T., Saino, T., 2004. Increased stratification and decreased lower trophic level productivity in the Oyashio region of the North Pacific: A 30-year retrospective study. J. Oceanogr. 60, 149–162.

Csanady, G.T., 1978. The arrested topography wave. J. Phys. Oceanogr. 8, 47–62.

Dai, A., Trenberth, K.E., 2002. Estimates of freshwater discharge from continents: Latitudinal and seasonal variations. J. Hydrometeorol. 3, 660–687.

Dee, D.P., Uppala, S.M., Simmons, A.J., Berrisford, P., Poli, P., Kobayashi, S., Andrae, U., Balmaseda, M.A., Balsamo, G., Bauer, P., Bechtold, P., Beljaars, A.C.M., van de Berg, L., Bidlot, J., Bormann, N., Delsol, C., Dragani, R., Fuentes, M., Geer, A.J., Haimberger, L., Healy, S.B., Hersbach, H., Hólm, E.V., Isaksen, L., Kållberg, P., Köhler, M., Matricardi, M., McNally, A.P., Monge-Sanz, B.M., Morcrette, J.J., Park, B.K., Peubey, C., de Rosnay, P., Tavolato, C., Thépaut, J.N., Vitart, F., 2011. The ERA-Interim reanalysis: configuration and performance of the data assimilation system. Q. J. R. Meteorolog. Soc. 137, 553–597.

Duce, R.A., Tindale, N.W., 1991. Atmospheric transport of iron and its deposition in the ocean. Limnol. Oceanogr. 36, 1715–1726.

Garcia, H.E., Locarnini, R.A., Boyer, T.P., Antonov, J.I., Zweng, M.M., Baranova, O.K., Johnson, D.R., 2010. World Ocean Atlas 2009: Nutrients (phosphate, nitrate, and silicate). In: Levitus, S. (Ed.), NOAA Atlas NESDIS 71, vol. 4, U.S. Government Printing Office, Washington, D.C, pp. 398.

Gradyshev, S., Talley, L., Kantakov, G., Khen, G., Wakatsuchi, M., 2003. Distribution, formation, and seasonal variability of Okhotsk Sea Mode Water. J. Geophys. Res. 108, 3186. https://doi.org/10.1029/2001JC000877.

Harrison, P.J., Boyd, P.W., Varela, D.E., Takeda, S., Shiomoto, A., Odate, T., 1999. Comparison of factors controlling phytoplankton productivity in the NE and NW subarctic Pacific gyres. Prog. Oceanogr. 43, 205–234.

Harrison, P.J., Whitney, F.A., Tsuda, A., Saito, H., Tadokoro, K., 2004. Nutrient and plankton dynamics in the NE and NW gyres of the subarctic Pacific Ocean. J. Oceanogr. 60, 93–117.

Hasumi, H., 2006. CCSR Ocean Component Model (COCO): version 4.0.

Hunke, E.C., Dukowicz, J.K., 1997. An elastic–viscous–plastic model for sea ice dynamics. J. Phys. Oceanogr. 27, 1849–1867.

Isoda, Y., Kuroda, H., Myousyo, T., Honda, S., 2003. Hydrographic feature of coastal Oyashio and its seasonal variation. Bull. Coast. Oceanogr. 41, 5–12 (in Japanese with English abstract).

Isoguchi, O., Kawamura, H., 2006. Seasonal to interannual variations of the western boundary current of the subarctic North Pacific by a combination of the altimeter and tide gauge sea levels. J. Geophys. Res. 111, C04013. https://doi.org/10.1029/2005JC003080.

Ito, S., Uehara, K., Miyao, T., Miyake, H., Yasuda, I., Watanabe, T., Shimizu, Y., 2004. Characteristics of SSH anomaly based on TOPEX/POSEIDON altimeter and in situ measured velocity and transport of Oyashio on OICE. J. Oceanogr. 60, 425–437.

Itoh, M., Ohshima, K.I., 2000. Seasonal variations of water masses and sea level in the southwestern part of the Okhotsk Sea. J. Oceanogr. 56, 643–654.

Itoh, S., Yasuda, I., 2010. Characteristics of mesoscale eddies in the Kuroshio-Oyashio Extension region detected from the distribution of the sea surface height anomaly. J. Phys. Oceanogr. 40, 1018–1034.

Kaplan, D., Glass, L., 1995. Understanding nonlinear dynamics. Springer-Verlag, p. 420.

Kara, A.B., Rochford, P.A., Hurlburt, H.E., 2000. Efficient and accurate bulk parameterizations of air–sea fluxes for use in general circulation models. J. Atmos. Oceanic Technol. 17, 1421–1438.

Kasai, H., Saito, H., Yoshimori, A., Taguchi, S., 1997. Variability in timing and magnitude of spring bloom in the Oyashio region, the western subarctic Pacific off Hokkaido, Japan. Fish. Oceanogr. 6, 118–129.

Kawamiya, M., Kishi, M.J., Suginohara, N., 2000. An ecosystem model for the North Pacific embedded in a general circulation model Part I: Model description and characteristics of spatial distributions of biological variables. J. Mar. Syst. 25, 129–157.

Kono, T., Kawasaki, Y., 1997. Modification of the western subarctic water by exchange with the Okhotsk Sea. Deep-Sea Res. I 44, 689–711.

Kono, T., Foreman, M., Chadler, P., Kawasaki, M., 2004. Coastal Oyashio south of Hokkaido, Japan. J. Phys. Oceanogr. 34, 1477–1494.

Kuroda, H., Wagawa, T., Kakehi, S., Shimizu, Y., Kusaka, A., Okunishi, T., Hasegawa, D., Ito, S., 2017. Long-term mean and seasonal variation of altimetry-derived Oyashio transport across the A-line off the southeastern coast of Hokkaido, Japan. Deep Sea Res. Part I 121, 95–109.

Kuroda, H., Toya, Y., Watanabe, T., Nishioka, J., Hasegawa, D., Taniuchi, Y., Kuwata, A., 2019. Influence of Coastal Oyashio water on massive spring diatom blooms in the Oyashio area of the North Pacific Ocean. Prog. Oceanogr. 175, 328–344.

Kusaka, A., Ono, T., Azumaya, T., Kasai, H., Oguma, S., Kawasaki, Y., Hirakawa, K., 2009. Seasonal variations of oceanographic conditions in the continental shelf area off the eastern Pacific coast of Hokkaido. Japan. *Oceanogr. in Japan* 18, 135–156 (in Japanese with English abstract).

Levitus, S., Boyer, T., 1994. World Ocean Atlas 1994: Temperature, NOAA Atlas NESDIS 4, vol. 4. National Oceanic and Atmospheric administration, Silver Spring, Md, pp. 150.

Linkin, M.E., Nigam, S., 2008. The North Pacific Oscillation–west Pacific teleconnection pattern: Mature-phase structure and winter impacts. J. Clim. 21, 1979–1997. https://doi.org/10.1175/2007JCLI2048.1.

Luo, C., Mahowald, N.M., del Corral, J., 2003. Sensitivity study of meteorological parameters on mineral aerosol mobilization, transport, and distribution. J. Geophys. Res. 108, 4447. https://doi.org/10.1029/2003JD003483, D15.

Mahowald, N., Baker, A., Bergametti, G., Brooks, N., Duce, R., Jickells, T., Kubilay, N., Prospero, J., Tegen, I., 2005. Atmospheric global dust cycle and iron inputs to the ocean. Global Biogeochem. Cycles 19, GB4025. https://doi.org/10.1029/2004GB002402.

Martin, J.H., Knauer, G.A., Karl, D.M., Broenkow, W.W., 1987. VERTEX: carbon cycling in the northeast Pacific. Deep Sea Res. Part I 34, 267–285. https://doi.org/10.1016/0198-0149(87)90086-0.

Matsuda, J., Mitsudera, H., Nakamura, T., Uchimoto, K., Nakanowatari, T., Ebuchi, N., 2009. Wind and buoyancy driven intermediate-layer overturning in the Sea of Okhotsk. *Deep-Sea Res. Part I.* 56, 1401–1418.

Mantua, N.J., Hare, S.R., Zhang, Y., Wallace, J.M., Francis, R.C., 1997. A Pacific interdecadal climate oscillation with impacts on salmon production. Bull. Am. Meteorol. Soc. 78, 1069–1079.

Measures, C.I., Brown, M.T., Vink, S., 2005. Dust deposition to the surface waters of the western and central North Pacific inferred from surface water dissolved aluminum concentrations. Geochem. Geophys. Geosyst. 6, Q09M03. https://doi.org/10.1029/2005GC000922.

Mensah, V., Ohshima, K.I., Nakanowatari, T., Riser, S., 2019. Seasonal changes of water mass, circulation and dynamic response in the Kuril Basin of the Sea of Okhotsk. Deep Sea Research Part I 144, 115–131.

Misumi, K., Tsumune, D., Yoshida, Y., Uchimoto, K., Nakamura, T., Nishioka, J., Mitsudera, H., Bryan, F.O., Lindsay, K., Moore, J.K., Doney, S.C., 2011. Mechanisms controlling dissolved iron distribution in the North Pacific: A model study. J. Geophys. Res. 116, G03005. https://doi.org/10.1029/2010JG001541.

Mizuta, G., Fukamachi, Y., Ohshima, K.I., Wakatsuchi, M., 2003. Structure and seasonal variability of the East Sakhalin Current. J. Phys. Oceanogr. 33, 2430–2445.

Nakamura, T., Awaji, T., 2004. Tidally induced diapycnal mixing in the Kuril Straits and its role in water transformation and transport: A three-dimensional nonhydrostatic model experiment. J. Geophys. Res.-Oceans 109, C09S07. https://doi.org/10.1029/2003JC001850.

Nakamura, T., Toyoda, T., Ishikawa, Y., Awaji, T., 2006. Enhanced ventilation in the Okhotsk Sea through tidal mixing at the Kuril Straits. Deep Sea Res. Part I 53, 425–448.

Nakanowatari, T., Ohshima, K.I., 2014. Coherent sea level variation in and around the Sea of Okhotsk. Prog. Oceanogr. 126, 58–70.

Nakanowatari, T., Nakamura, T., Uchimoto, K., Uehara, H., Mitsudera, H., Ohshima, K.I., Hasumi, H., Wakatsuchi, M., 2015. Causes of the multidecadal-scale warming of the intermediate water in the Okhotsk Sea and western subarctic North Pacific. J. Clim. 28, 714–736.

Nakanowatari, T., Nakamura, T., Uchimoto, K., Nishioka, J., Mitsudera, H., Wakatsuchi, M., 2017. Importance of Ekman transport and gyre circulation change on seasonal variation of surface dissolved iron in the western subarctic North Pacific. J. Geophys. Res. Oceans 122. https://doi.org/10.1002/2016JC012354.

Nishioka, J., Ono, T., Saito, H., Nakatsuka, T., Takeda, S., Yoshimura, T., Suzuki, K., Kuma, K., Nakabayashi, S., Tsumune, D., Mitsudera, H., Johnson, W.K., Tsuda, A., 2007. Iron supply to the western subarctic Pacific: Importance of iron export from the Sea of Okhotsk. J. Geophys. Res. 112, C10012. https://doi.org/10.1029/2006JC004055.

Nishioka, J., Ono, T., Saito, H., Sakaoka, K., Yoshimura, T., 2011. Oceanic iron supply mechanisms which support the spring diatom bloom in the Oyashio region, western subarctic Pacific. J. Geophys. Res. 116, C02021. https://doi.org/10.1029/2010JC006321.

Nishioka, J., Nakatsuka, T., Watanabe, Y.W., Yasuda, I., Kuma, K., Ogawa, H., Ebuchi, N., Scherbini, A., Volkov, Y.N., Shiraiwa, T., Wakatsuchi, M., 2013. Intensive mixing along an island chain controls oceanic biogeochemical cycles. Global Biogeochem. Cycles 27, 1–10. https://doi.org/10.1002/gbc.20088.

Nosaka, Y., Yamashita, Y., Suzuki, K., 2017. Dynamics and origin of transparent exopolymer particles in the Oyashio region of the western subarctic Pacific during the spring diatom bloom. Front. Mar. Sci. 4, 79.

Ohshima, K.I., Riser, S.C., Wakatsuchi, M., 2005. Mixed layer evolution in the Sea of Okhotsk observed with profiling floats and its relation to sea ice formation. Geophys. Res. Lett. 32, L06607. https://doi.org/10.1029/2004GL021823.

Okamoto, S., Hirawake, T., Saitoh, S.-I., 2010. Interannual variability in the magnitude and timing of the spring bloom in the Oyashio region. Deep Sea Res. Part II 57, 1608–1617.

Ono, T., Midorikawa, T., Watanabe, Y.W., Tadokoro, K., Saino, T., 2001. Temporal increases of phosphate and apparent oxygen utilization in the subsurface waters of western subarctic Pacific from 1968 to 1998. Geophys. Res. Lett. 28, 3285–3288.

Ono, T., Tadokoro, K., Midorikawa, T., Nishioka, J., Saino, T., 2002. Multi-decadal decrease of net community production in western subarctic North Pacific. Geophys. Res. Lett. 29, 27-1-27-4.

Osafune, S., Yasuda, I., 2006. Bidecadal variability in the intermediate waters of the northwestern subarctic Pacific and the Okhotsk Sea in relation to 18.6-year period nodal tidal cycle. J. Geophys. Res. 111, C05007. https://doi.org/10.1029/2005JC003277.

Parekh, P., Follows, M.J., Boyle, E.A., 2005. Decoupling of iron and phosphate in the global ocean. Global Biogeochem. Cycles 19. https://doi.org/10.1029/2004GB002280.

Perovich, D.K., 1998. The optical properties of sea ice. In: Lepparanta, M.Ed. (Ed.), Physics of Ice-covered Seas, vol. 1. Helsinki University Press, pp. 195–230.

Pugh, D.T., 1987. Tides, surges, and mean sea-level. Wiley, Chichester, New York.

Saito, H., Tsuda, A., Kasai, H., 2002. Nutrient and plankton dynamics in the Oyashio region of the western subarctic Pacific. Deep-Sea Res. II 49, 5463–5486.

Sakamoto, K., Tsujino, H., Nishikawa, S., Nakano, H., Motoi, T., 2010. Dynamics of the coastal Oyashio and its seasonal variation in a high-resolution western North Pacific ocean model. J. Phys. Oceanogr. 40, 1283–1301.

Sakurai, Y., 2007. An overview of the Oyashio ecosystem. Prog. Oceanogr. 54, 23–26.

Semtner, A.J., 1976. Model for thermodynamic growth of sea ice in numerical investigations of climate. J. Phys. Oceanogr. 6, 379–389.

Stephens, C., Antonov, J.I., Boyer, T.P., Conkright, M.E., Locarnini, R.A., O'Brien, T.D., Garcia, H.E., 2002. World Ocean Atlas 2001: Temperature. NOAA Atlas NESDIS 49 vol. 1, 176.

Suzuki, K., Kuwata, A., Yoshie, N., Shibata, A., Kawanobe, K., Saito, H., 2011. Population dynamics of phytoplankton, heterotrophic bacteria, and viruses during the spring bloom in the western subarctic Pacific. Deep-Sea Res. Part I-Oceanogr. Res. Papers 58, 575–589.

Tadokoro, K., Chiba, S., Ono, T., Midorikawa, T., Saino, T., 2005. Interannual variation in *Neocalanus* biomass in the Oyashio waters of the western North Pacific. Fish. Oceanogr. 14, 210–222.

Tadokoro, K., Ono, T., Yasuda, I., Osafune, S., Shiomoto, A., Sugisaki, H., 2009. Possible mechanisms of decadal-scale variation in $PO_4$ concentration in the western North Pacific. Geophys. Res. Lett. 36, L08606. https://doi.org/10.1029/2009GL037327.

Takahashi, T., Sutherland, S.C., Sweeney, C., Poisson, A., Metzl, N., Tilbrook, B., Bates, N., Wanninkhof, R., Feely, R.A., Sabine, C., Olafsson, J., Nojiri, Y., 2002. Global sea–air CO2 flux based on climatological surface ocean pCO(2), and seasonal biological and temperature effects. Deep-Sea Res. Part I-Top. Stud. Oceanogr. 49, 1601–1622.

Takata, H., 2005. Comparative vertical distributions of iron in the Japan Sea, the Bering Sea, and the western North Pacific Ocean. J. Geophys. Res. 110, C07004. https://doi.org/10.1029/2004JC002783.

Takata, H., Kuma, K., Isoda, Y., Otosaka, S., Senjyu, T., Minagawa, M., 2008. Iron in the Japan Sea and its implications for the physical processes in deep water. Geophys. Res. Lett. 35, L02606. https://doi.org/10.1029/2007GL031794.

Talley, L.D., 1991. An Okhotsk Sea water anomaly: Implications for ventilation in the North Pacific. Deep Sea Res., Part A 38(suppl.), S171–S190.

Tanaka, Y., Hibiya, T., Niwa, Y., Iwamae, N., 2010. Numerical study of K1 internal tides in the Kuril Straits. J. Geophys. Res. 115, C09016. https://doi.org/10.1029/2009JC005903.

Taniguchi, A., 1999. Differences in the structure of the lower trophic levels of pelagic ecosystems in the eastern and western subarctic Pacific. Prog. Oceanogr. 43, 289–315.

Trenberth, K.E., Hurrell, J.W., 1994. Decadal atmosphere–ocean variations in the Pacific. Clim. Dyn. 9, 303–319.

Tsuda, A., Takeda, S., Saito, H., Nishioka, J., Nojiri, Y., Kudo, I., Kiyosawa, H., Shiomoto, A., Imai, K., Ono, T., Shimamoto, A., Tsumune, D., Yoshimura, T., Aono, T., Hinuma, A., Kinugasa, M., Suzuki, K., Sohrin, Y., Noiri, Y., Tani, H., Deguchi, Y., Tsurushima, N., Ogawa, H., Fukami, K., Kuma, K., Saino, T., 2003. A mesoscale iron enrichment in the western subarctic Pacific induces large centric diatom bloom. Science 300, 958–961.

Tsuda, A., Kiyosawa, H., Kuwata, A., Mochizuki, M., Shiga, N., Saito, H., Chiba, S., Imai, K., Nishioka, J., Ono, T., 2005. Responses of diatoms to iron-enrichment (SEEDS) in the western subarctic Pacific, temporal and spatial comparisons. Prog. Oceanogr. 64, 189–205.

Uchimoto, K., Nakamura, T., Nishioka, J., Mitsudera, H., Yamamoto-Kawai, M., Misumi, K., Tsumune, D., 2011. Simulations of chlorofluorocarbons in and around the Sea of Okhotsk: Effects of tidal mixing and brine rejection on the ventilation. J. Geophys. Res. 116, C02034. https://doi.org/10.1029/2010JC006487.

Uchimoto, K., Nakamura, T., Nishioka, J., Mitsudera, H., Misumi, K., Tsumune, D., Wakatsuchi, M., 2014. Simulation of high concentration of iron in dense shelf water in the Okhotsk Sea. Prog. Oceanogr. 126, 194–210.

Uehara, H., Kruts, A.A., Mitsudera, H., Nakamura, T., Volkov, Y.N., Wakatsuchi, M., 2014. Remotely propagating salinity anomaly varies the source of the North Pacific ventilation. Prog. Oceanogr. 126, 80–97. https://doi.org/10.1016/j.pocean.2014.04.016.

Wong, C.S., Matear, R.J., Freeland, H.J., Whitney, F.A., Bychkov, A.S., 1998. WOCE line P1W in the Sea of Okhotsk: 2. CFCs and the formation rate of intermediate water. J. Geophys. Res. 103, 15625–15642.

Woodworth, P.L., 1991. The permanent service for mean sea level and the global sea level observing system. J. Coastal Res. 7, 699–710.

Yasunaka, S., Ono, T., Nojiri, Y., Whitney, F.A., Wada, C., Murata, A., Nakaoka, S., Hosoda, S., 2016. Long-term variability of surface nutrient concentrations in the North Pacific. Geophys. Res. Lett. 43, 3389–3397.

Yoshida, T., 1992. Climatological seasonal variations of the distribution of Oyashio cold water. Umi to Sora 68, 79–88 (in Japanese with English abstract).